HHS Public Access

Author manuscript

Cell. Author manuscript; available in PMC 2022 October 28.

Published in final edited form as:

Cell. 2021 October 28; 184(22): 5622–5634.e25. doi:10.1016/j.cell.2021.09.013.

Bombesin-like peptide recruits disinhibitory cortical circuits and enhances fear memories

Sarah Melzer[1], **Elena R Newmark**[1], **Grace Or Mizuno**[2], **Minsuk Hyun**[1], **Adrienne C. Philson**[1], **Eleonora Quiroli**[1], **Beatrice Righetti**[1], **Malika R. Gregory**[1], **Kee Wui Huang**[1], **James Levasseur**[1], **Lin Tian**[1], **Bernardo L. Sabatini**[1,*]

[1]Dept. of Neurobiology, Howard Hughes Medical Institute, Harvard Medical School, 220 Longwood Ave, Boston, Massachusetts 02115, USA

[2]Departments of Biochemistry and Molecular Medicine, School of Medicine, University of California, Davis, Davis, CA, USA

Summary

Disinhibitory neurons throughout the mammalian cortex are powerful enhancers of circuit excitability and plasticity. The differential expression of neuropeptide receptors in disinhibitory, inhibitory and excitatory neurons suggests that each circuit motif may be controlled by distinct neuropeptidergic systems. Here, we reveal that a bombesin-like neuropeptide, gastrin-releasing peptide (GRP), recruits disinhibitory cortical microcircuits through selective targeting and activation of vasoactive intestinal peptide (VIP)-expressing cells. Using a genetically-encoded GRP sensor, optogenetic anterograde stimulation and trans-synaptic tracing we reveal that GRP regulates VIP cells most likely via extrasynaptic diffusion from several local and long-range sources. *In vivo* photometry and CRISPR/Cas9-mediated knockout of the GRP receptor (GRPR) in auditory cortex indicate that VIP cells are strongly recruited by novel sounds and aversive shocks, and that GRP-GRPR signaling enhances auditory fear memories. Our data establish peptidergic recruitment of selective disinhibitory cortical microcircuits as a mechanism to regulate fear memories.

Graphical Abstract

Correspondence: bsabatini@hms.harvard.edu.
*Lead Contact

AUTHOR CONTRIBUTIONS

Conceptualization, S.M. and B.L.S.; Methodology, S.M., B.L.S., L.T., K.W.H., M.H.; Formal Analysis, S.M., E.R.N., A.C.P, L.T.; Investigation, S.M., E.R.N., G.O.M, M.H., A.C.P, E.Q., B.R., M.R.G.; Resources, K.W.H., J.L.; Writing, S.M., B.L.S.; Visualization, S.M., E.R.N., L.T., B.L.S.; Supervision, S.M., B.L.S., L.T.; Funding Acquisition, B.L.S., L.T., S.M..

DECLARATION OF INTERESTS

L.T. and G.O.M. are co-founders of Seven Biosciences.

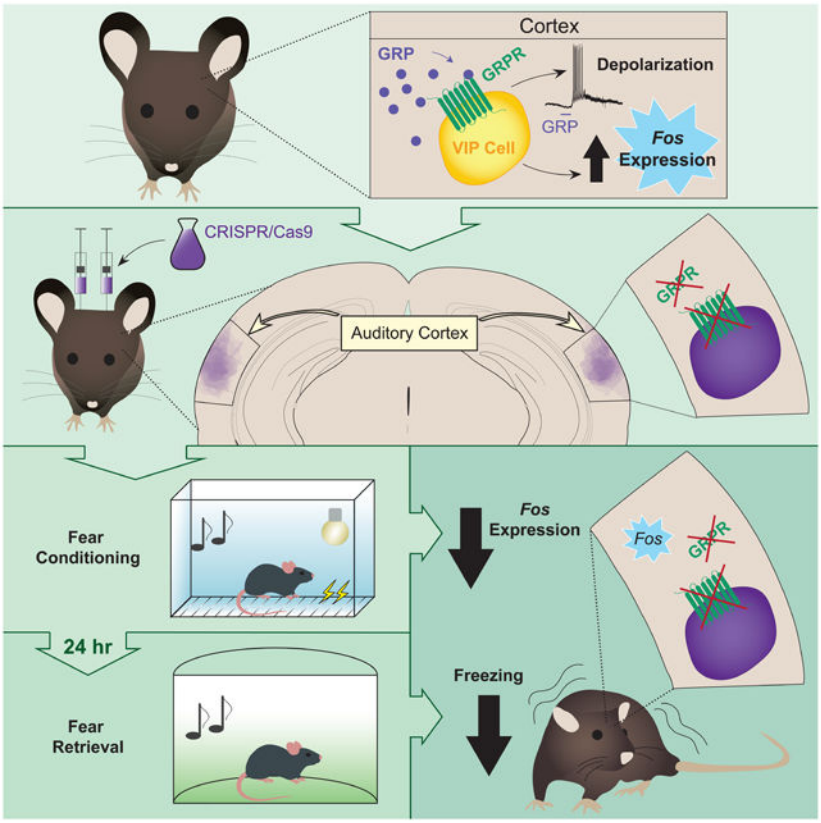

ETOC:

Critical function of neuropeptides in cortex-dependent behaviors is demonstrated by local and long-range sources of the neuropeptide, GRP, selectively recruiting disinhibitory cortical microcircuts in auditory cortex to regulate fear memories in mice.

Keywords

Gastrin-releasing peptide; neuropeptide; cortex; fear memory; VIP cells; disinhibition; CRISPR/Cas9

Introduction

Cortical circuits consist of multiple cell classes whose orchestrated activity is crucial for signal processing and plasticity. The post-synaptic specificity of afferent and intracortical inputs permits the temporally precise regulation of different cortical cell classes during behavior (Karnani et al., 2016; Pfeffer et al., 2013; Pi et al., 2013). For example, cortical inputs facilitate neuronal mismatch responses (Leinweber et al., 2017), suppress responses to predicted and unattended stimuli (Iurilli et al., 2012), or enhance sensory responses and plasticity (Fu et al., 2014, 2015; Lee et al., 2013; Zhang et al., 2014) by targeting mainly excitatory, inhibitory or disinhibitory cortical neurons, respectively. Thus, cortical circuit motifs are regulatory control points that can be differentially activated to induce behaviorally-relevant changes in cortical state.

The specificity of the expression of receptors for neuromodulators, signaling molecules that often act through slower extrasynaptic transmission, suggests that multiple channels of cortical neuromodulator-based communication exist that also regulate functionally-relevant network activity (Marlin et al., 2015; Nakajima et al., 2014; Smith et al., 2019; Tasic et al., 2016). Nevertheless, most cortical neuropeptides have not been investigated with respect to their cellular and behavioral effects.

Within cortex, vasoactive-intestinal peptide (VIP)-expressing neurons, due to their synaptic targets, are well-positioned to control circuit excitability and plasticity (Adler et al., 2019; Batista-Brito et al., 2017; Fu et al., 2014, 2015; Karnani et al., 2016; Pfeffer et al., 2013; Pi et al., 2013). VIP cells express a diverse set of neuromodulator receptors (Smith et al., 2019; Tasic et al., 2016, 2018), making them likely targets of local and long-range neuromodulatory systems.

One neuromodulator with unknown function in most cortical brain areas is gastrin-releasing peptide (GRP), a bombesin-like peptide that binds to the G protein-coupled GRP receptor (GRPR) with high affinity and selectivity (Kroog et al., 1995). GRP release in different parts of the central nervous system mediates itch (Sun and Chen, 2007) and sighing (Li et al., 2016b), and has been implicated in fear memories (Mountney et al., 2006, 2008; Roesler et al., 2003).

Here we identify GRPR as a regulator of VIP cell-dependent signaling and behavior. We demonstrate that GRPR is expressed nearly exclusively in VIP cells in many cortical regions. Endogenous GRPR signaling during fear conditioning induces immediate early gene (IEG) expression in VIP cells, consistent with a role for GRP in facilitating excitability. Furthermore, CRIPSR/Cas9-mediated and conditional knockout (KO) of GRPR in auditory cortex (ACx) diminishes fear memories in control but not GRP KO mice in a discriminatory auditory fear conditioning task (Letzkus et al., 2011) that engages VIP cells in a cue- and novelty-dependent manner. Our results thus highlight the importance of neuropeptidergic cell type-specific communication channels in regulating functionally relevant cortical circuits.

Results

Cortex-wide expression of GRP and its receptor

To identify candidate neuromodulator receptors for selective regulation of VIP cells, we analyzed gene expression in mouse visual cortex in two single-cell (sc) RNA sequencing datasets (Tasic et al., 2016, 2018) and identified the gastrin-releasing peptide receptor (*Grpr,* Fig. S1A) as a candidate for VIP cell-specific peptidergic neuromodulation (as proposed previously (Smith et al., 2019)). Fluorescent *in situ* hybridization (FISH) targeting the gene encoding its specific ligand, gastrin-releasing peptide (Grp), revealed mRNA expression in 28±5% of glutamatergic cells across cortex (96±0% of Grp^+ cells were $Slc17a6/7/8^+$ whereas only 3±0% were *Gad1/2,* Fig. 1A-C and E-F, Fig. S1B-C). Furthermore, *Grpr* expression was detected in 81±2% of Vip^+ cells, and 83±3% of $Grpr^+$ cells expressed *Vip* (Fig. 1D-F, Fig. S1D). Similar numbers were found during early postnatal development

(Fig. S1E) suggesting preserved GRPR-mediated signaling throughout development and adulthood.

Since 19% of *Grpr*$^+$ cells were *Vip*-negative GABAergic neurons (Fig. 1F), we examined whether *Grpr* is present in other major inhibitory cell types and detected *Sst* and *Pvalb* expression in a subset of *Grpr*$^+$ cells (Fig. S1F). In contrast, in the adult mouse hippocampus, an area with comparably high levels of *Grpr,* expression was relatively evenly distributed among the three major GABAergic cell types (Fig. S1G), suggesting that preferential VIP cell targeting by GRP is a brain area-dependent feature.

Several neuropeptidergic systems are evolutionarily conserved (Jékely et al., 2018), raising the question as to whether GRPR signaling follows similar principles in human cortex as in mouse. Indeed, FISH in the human visual cortex (BA17) showed that a large proportion of *GRPR*$^+$ cells expressed *VIP* and *GAD1,* but rarely SST and *PVALB* (Fig. 1G-I, Fig. S1H), suggesting that the neocortical GRP-GRPR signaling pathway is evolutionarily conserved between mouse and human. The large fraction of human *GRPR*$^+$ cells that lack *VIP* expression may represent a distinct GABAergic *VIP/SST/PVALB*-negative cell class or cells in which *VIP* mRNA levels are below detection threshold. Consistent with the former, scRNA sequencing data show expression of *GRPR* in *LAMP1*$^+$ putative layer 1 neurons (Hodge et al., 2019) which are thought to have a disinhibitory function analogous to that of VIP cells (Letzkus et al., 2011).

Putative local and long-range sources of GRP

The patterns of expression of *Grp* suggest that it is expressed by cortico-cortical or cortico-thalamic neurons, both of which reside in L6 (Briggs and Usrey, 2011). To identify cortico-thalamic neurons, we injected Cholera Toxin B (CTB) into the auditory thalamus (Fig. 2A-B). FISH revealed that 86±4% of *Grp*$^+$ cells in L6 were retrogradely labeled with CTB (n=958 *Grp*$^+$ cells in 4 hemispheres) and that L6 *Grp*$^+$ neurons constitute a subpopulation of cortico-thalamic neurons (41±10% out of 1494 CTB$^+$ cells in 4 hemispheres; Fig. 2C). Similar results were obtained after injections into the motor thalamus (Fig. S2A), establishing L6 cortico-thalamic neurons as a putative source of cortical GRP signaling.

We also detected strong *Grp* expression in several input areas of the ACx including the lateral amygdala (LA), contralateral ACx (clACx,) temporal association area (TeA), perirhinal cortex (Per) and auditory thalamic nuclei including the medial part of the medial geniculate nucleus (MGM) and the suprageniculate nucleus (SG), suggesting that these might be sources of cortical GRP. To examine this possibility, we injected CTB into the ACx (Fig. 2D) and analyzed *Grp* expression by FISH (Fig. 2E, Fig. S2B-C). Indeed, the majority of CTB$^+$ cells in the LA and about half of the CTB$^+$ cells in the thalamus and in Per were *Grp*$^+$. Less coexpression occured in the TeA and clACx. In each area, only a small population of *Grp*$^+$ cells were CTB$^+$ (Fig. 2E), suggesting that a subset of *Grp*$^+$ cells are putative long-range sources of GRP in cortex.

Whereas fast synaptic neurotransmission typically occurs between specific subsets of directly connected neurons, extrasynaptic diffusion of neuropeptides may allow these neuromodulators to reach all cells in a target region. To test whether VIP cells receive

synaptic inputs and peptidergic signals from overlapping or distinct subsets of neurons, we used pseudotyped rabies virus (RabV) transsynaptic retrograde labeling from ACx VIP cells (Fig. 2F-G, Fig. S2D-E). Only a small subpopulation of retrogradely-labeled neurons expressed *Grp* in ACx and posterior portions of the auditory thalamus (Fig. 2H-I, Fig. S2F). Similar results were obtained after injections into M1 (Fig. S2G-H), suggesting that VIP cells across multiple cortical areas receive GRP signals from a neuronal population that is largely distinct from that which provides direct synaptic input (Fig. 2J).

To confirm these results, we optogenetically stimulated amygdalo-cortical projections, a majority of which are Grp^{+} (Fig. S2I), and examined evoked excitatory postsynaptic currents (EPSCs) in L2/3 VIP cells and neighboring pyramidal (Pyr) cells in the primary ACx using whole-cell recordings. Consistent with our retrograde labeling results, the majority of ACx cells did not receive direct synaptic inputs (Fig. S2J). This was not due to a failure to efficiently activate axonal projections, since most VIP and Pyr cells recorded in L2/3 of the TeA within the same brain slices received strong synaptic inputs (Fig. S2J).

Extrasynaptic GRP signaling requires that the peptide be stable and efficiently diffuse through extracellular space. To monitor GRP diffusion *in vivo,* we developed a genetically-encoded GRP sensor (grpLight) based on a previously established platform (Patriarchi et al., 2018) (Fig. S2K-M). GrpLight showed high specificity for GRP compared to other common neuropeptides and could detect nanomolar concentrations of GRP (Fig. S2N-Q). *In vivo* photometric imaging of grpLight green fluorescence in the ACx following infusion of red fluorescently-tagged GRP (TAMRA-GRP) into a distant cortical area revealed long-lasting increases minutes after the start of GRP infusion (Fig. S2R-T). Our results show that GRP diffuses slowly and maintains biological activity for over an hour in intact brain tissue, suggesting that GRP is a long-acting peptide that reaches large neuronal populations through extrasynaptic diffusion.

GRP depolarizes and increases intracellular Ca^{2+} in cortical VIP cells

The cell type specificity of *Grpr* expression suggests that VIP cells are the primary targets of modulation by GRP. Whole-cell current-clamp recordings in ACx VIP cells (using *Vip*-EGFP mice) of male mice revealed that most VIP cells (7 out of 10) depolarize upon GRP bath application (300 nM for 2 min), occasionally resulting in long-lasting (>1 min) burst-like firing activity (3 out of 10 neurons, Fig. 3A-B, Fig. S3A-B). Depolarization was concentration-dependent (Fig. 3C) and strongly reduced by a GRPR antagonist (Fig. S3B). As the *Grpr* gene is on the X-chromosome, we separately examined VIP cell responses in female mice and found a non-significantly larger depolarization compared to male mice (Fig. S3C). Similar results were obtained in M1 (Fig. S3E).

To confirm that the effects of GRP are largely VIP cell-specific, we obtained current-clamp recordings from SST, PVALB and Pyr cells in the ACx (Fig. 3D) and M1 (Fig. S3F). GRP-evoked depolarizations in all three cell types were significantly smaller than in VIP cells (Fig. 3E and Fig. S3G). No significant difference was found between PVALB cell depolarizations upon GRP application and in control recordings without GRP (Fig. S3D), confirming that VIP cells are the preferential target of GRP.

The GRP-evoked subthreshold depolarization of most VIP cells in cortex suggests that GRPR signaling increases excitability in these cells. Indeed, GRP bath application significantly increased the evoked spike probability of VIP cells in response to optogenetic stimulation of thalamo-cortical afferents without increasing spontaneous spike rate prior to stimulation onset (Fig. S3H).

Previous reports suggested that GRPR is a $G\alpha_q$-coupled receptor (Hellmich 1997). A common secondary messenger of $G\alpha_q$ signaling is intracellular calcium (Ca^{2+}). To visualize Ca^{2+} dynamics and facilitate the identification of VIP cells in acute slices, we coexpressed the large-stokes shift red fluorophore mBeRFP (Yang et al., 2013) stoichiometrically with GCaMP using a self-cleaving P2A peptide linker (Fig. 3F). Bath application of GRP increased GCaMP fluorescence in most VIP cells in ACx of male and female mice and in M1 at concentrations as low as 3 nM (Fig. 3G-H, Fig. S3I-J). Reminiscent of the GRP-induced burst activity in some VIP cells (Fig. 3B, Fig. S3E), GCaMP fluorescence exhibited non-synchronized phasic (oscillatory) fluctuations at various frequencies in 26% of imaged VIP cells (Fig. 3H-I, Fig. S3K) that were partially blocked by TTX (14% of cells with Ca^{2+} oscillations; Fig. 3I, Fig. S3L-M), suggesting that the majority of GRP-induced Ca^{2+} signaling is AP-dependent. The AP-independent Ca^{2+} elevations are consistent with regulation of intracellular Ca^{2+} release from internal stores by $G\alpha_q$- and IP_3-mediated signaling. The delay between GRP application and changes in intracellular Ca^{2+} were largely due to delays in the infusion system (Fig. S3N). In summary, our data indicate that GRP is a selective modulator of VIP cell signaling. Unfortunately, grpLight is not able to detect functionally relevant GRP levels *in vivo* as analysis of intracellular Ca^{2+} in VIP cells shows that GRP infusion has functional effects on these cells *in vivo* well before photometric detection of changes in grpLight fluorescence (Fig. S3O).

GRP disinhibits cortex and induces IEG expression

The main circuit effect of VIP cell activation in the cortex is inhibition of SST and PVALB cells (Karnani et al., 2016; Pi et al., 2013) (Fig. 4A). To test whether GRP leads to similar network effects, we recorded inhibitory postsynaptic currents (IPSCs) in SST and PVALB cells in acute ACx slices (Fig. 4B-C). Bath application of GRP increased IPSC frequencies in 60% of SST and 40% of PVALB cells in a TTX-sensitive manner. IPSC frequencies increased only in 1 out of 10 Pyr cells, consistent with sporadic direct inhibition of Pyr cells by VIP cells (Chiu et al., 2018). Similar effects were observed in M1 (Fig. S4A-B). EPSC frequency was hardly affected (Fig. S4C), suggesting that inhibition of SST cells is the main direct network effect of GRP-mediated VIP cell activation.

Since VIP cell-mediated disinhibition of Pyr cells strongly depends on the activity level of SST cells, we examined GRP-mediated disinhibition of Pyr cells *in vivo*. To this end, we injected GRP into M1 of anaesthetized mice and used expression of the IEG *Fos* as an indicator of neuronal activity (Sheng et al., 1990). We revealed a strong increase in Fos (*Fos*) expression ipsilateral to the injection site (Fig. 4D, Fig. S4D) in *Vip*$^+$ and glutamatergic cells across most cortical layers, without changes in expression in *Sst*$^+$ and *Pvalb*$^+$ cells (Fig. 4E-G and Fig. S4D_{1-2}). Importantly, GRP injections into M1 of mice lacking GRPR specifically in VIP cells (*Vip-IRES-Cre;Grpr*$^{fl/y}$ (Yu et al., 2017); Fig.

S4E$_{1-2}$) or injections of the diluent (NRR) alone (Fig. S4F$_{1-2}$) led to significantly smaller increases in *Fos* expression (Fig. S4G). A previous study indicated that *Fos* expression can be induced by a broad range of neuromodulatory inputs, whereas expression of another IEG, *Npas4,* is more tightly regulated by neuronal activity (Lin et al., 2008). We found that GRP injections lead to similar changes in *Npas4* levels, with significantly increased expression in *Vip*$^+$ and glutamatergic cells, but not *Sst*$^+$ and *Pvalb*$^+$ cells (Fig. 4H, Fig. S4D$_3$). *Npas4* expression was significantly smaller when GRP was injected into *Vip-IRES-Cre;Grpr*$^{fl/y}$ mice (Fig. S4E$_3$-G), confirming GRP-mediated disinhibition of glutamatergic cells through VIP cell-specific GRPR signaling.

ACx VIP cell activity encodes novel sounds and shocks during fear conditioning

The presence of *Grp*$^+$ cortically-projecting neurons in all areas of the thalamo-cortico-amygdala loop, a circuit central for the encoding of fear memories (Boatman and Kim, 2006), together with previous reports of stress- and fear-induced GRP release in the amygdala (Merali et al., 1998; Mountney et al., 2011) suggest that GRP modulates sensory processing in cortex in the presence of aversive cues. An ideal behavioral paradigm to examine this possibility is auditory discriminatory fear conditioning (Dalmay et al., 2019; Letzkus et al., 2011). Unlike many tasks that depend on simple sounds, memory in this task requires activity in ACx and is modulated by disinhibitory circuits (Dalmay et al., 2019; Letzkus et al., 2011).

To determine whether VIP cells in the ACx are recruited during this task, we recorded bulk Ca^{2+}-dependent fluorescence changes using fiber photometry. To optimize comparison of VIP cell activity across mice and behavioral sessions, we tested the suitability of the GCaMP6s-P2A-mBeRFP construct for quantitative analysis of GCaMP fluorescence *in vivo.* Characterization of emission spectrum, Ca^{2+}-sensitivity, and relative expression levels, as well as physiological properties of VIP cells expressing GCaMP-P2A-mBeRFP (Fig. 5A-G, Fig. S5A-E) confirmed that mBeRFP can be used as a reference to normalize GCaMP fluorescence and to detect movement artifacts and patchcord detachment or entanglement.

We acquired fiber-photometric recordings in GCaMP6s-P2A-mBeRFP-expressing VIP cells in the right ACx during fear conditioning (Fig. 5H, Fig. S5F-I). We observed strong fluorescence increases in VIP cells in response to novel conditioned (CS^+) and unconditioned (CS^-) sounds and foot shocks (Fig. 5H). The responses were not due to movement artifacts as demonstrated by stable mBeRFP fluorescence (Fig. S5J). The strong initial activation upon foot shocks, which triggered fast escape behavior, raise the possibility that VIP cell activity may be correlated with locomotion. However, neither the trial-averaged fluorescence during movement initiation after bouts of freezing nor cross-correlation of GCaMP fluorescence and speed revealed strong GCaMP modulation by locomotion (Fig. S5K-L).

To test how GRP modulates the VIP cell dynamics *in vivo,* we compared GCaMP fluorescence in response to novel sounds- and shocks before and following local infusion of GRP via a cannula. GRP increased peak responses of VIP cells to sounds and shocks without increasing discriminability between different stimuli (Fig. 5I, Fig. S5M), suggesting a function in cortical state modulation rather than stimulus-specific encoding.

GRPR signaling in the ACx enhances fear memories

To test whether GRP/GRPR signaling contributes to the modulation of fear memories, we used CRISPR/Cas9-mediated KO of *Grpr* (Fig. 6A). The efficiency of *Grpr* KO was confirmed by Ca^{2+} imaging in ACx VIP cells (Fig. 6B, Fig. S6A). Bilateral AAV-mediated CRISPR/Cas9 injections into the ACx of male wild type mice resulted in SaCas9-HA expression mainly in ACx (Fig. 6C, Fig. S6B-C). Electrophysiological analysis of ACx VIP cells did not reveal any significant changes in basic physiological parameters (Fig. S6D-E), suggesting that VIP cells are healthy and do not develop intrinsic compensatory mechanisms when GRPR is ablated. Fear conditioning of ctrl and KO mice increased freezing during CS^+ and CS^- throughout the conditioning session in both groups (Fig. 6D). 24 hrs after conditioning, mice were subjected to auditory fear memory retrieval. Freezing levels during CS^+ and CS^- were significantly reduced in KO mice compared to ctrl mice (Fig. 6E-F, Fig. S6F), indicating a function of GRPR signaling in enhancing cortex-dependent memory formation.

Neither the absolute freezing difference between CS^+ and CS^- (2-sample t-test: $t(28)=1.59$, $p=0.12$) nor the discrimination index (STAR Methods) were significantly different in ctrl and KO mice (Fig. 6G), indicating that the behavioral effect is not due to an impairment in auditory discrimination. Since freezing levels did not change significantly over time and freezing levels in KO mice were strongly reduced even during the first 4 CS^+ and CS^- (Fig. S6G-H), we conclude that the reduced freezing in KO mice is not due to accelerated fear extinction. Moreover, reduced freezing levels in KO mice were not purely a result of increased baseline freezing, since freezing levels were still significantly reduced in KO mice after subtraction of baseline freezing (Fig. S6I).

Importantly, ctrl and KO mice exhibited comparable locomotion during the conditioning session at baseline, during the first sounds and in response to the first foot shock (Fig. S6J-K), indicating that the reduced freezing level in KO mice was not a result of different pain sensitivity or overall activity levels.

To verify that the behavioral effects were due to GRP-GRPR signaling and not ligand-independent recruitment of GRPR signaling, we injected CRISPR/Cas9 constructs into $Grp^{-/-}$ KO mice and subjected mice to the same behavioral testing paradigm. Freezing levels during CS^+ and CS^- were not significantly different in $Grp^{-/-}$ mice injected with CRISPR/Cas9 constructs targeting *Grpr* or ctrl sequences (Fig. 6H, Fig. S6L-M), indicating that GRP signaling is required for the behavioral effects of GRPR. Importantly, *Grpr*-*Vip* coexpression was maintained in $Grp^{-/-}$ KO mice (Fig. S6N), confirming that the absence of behavioral effects was not due to a lack of GRPR expression in VIP cells of $Grp^{-/-}$ KO mice.

To further exclude that the observed behavioral effects were due to side effects, we repeated the behavioral experiments using conditional *Grpr* KO mice (Yu et al., 2017). We validated Cre-dependent KO of *Grpr* in these mice using Ca^{2+} imaging (Fig. 7A). To KO *Grpr* specifically in the ACx, we injected AAV hSyn-Cre-mCherry bilaterally into the ACx of $Grpr^{fl/y}$ (KO) or $Grpr^{wt/y}$ (ctrl) mice (Fig. 7B, Fig. S7A). Four weeks after injection, both groups of mice were exposed to fear conditioning and retrieval as above. Freezing levels in KO mice upon presentation of CS^+ and CS^- during retrieval were significantly reduced, with

no significant effect on auditory discrimination (Fig. 7C-D, Fig. S7B-C). Importantly, the reduced freezing levels in KO mice were not caused by differences in genetic background of *Grpr*$^{fl/y}$ and *Grpr*$^{wt/y}$ mice, since freezing levels in uninjected *Grpr*$^{fl/y}$ mice were not different from their ctrl littermates (Fig. S7D-E), confirming that *Grpr* KO in the ACx reduces fear-induced freezing in a discriminatory auditory fear conditioning paradigm.

To examine the functional and context-dependent implications of GRP-GRPR signaling for VIP cells *in vivo*, we quantified *Fos* expression in ACx *Vip*$^{+}$ cells three weeks after AAV-mediated injections of CRISPR/Cas9 constructs into the ACx of wild type mice. *Fos* expression in *Vip*$^{+}$ cells lacking GRPR was significantly lower than in ctrl cells directly after fear conditioning but not in naïve mice (Fig. S7F-G), consistent with context-dependent recruitment of endogenous GRPR signaling. In line with this finding, amygdalo-cortical and thalamo-cortical projection neurons, a majority of which expresses *Grp* (Fig. 2E), activated reliably during shocks (and during sounds in the case of thalamic projections) (Fig. 7E-F, Fig. S7H-I) consistent with context-dependent activation of GRP^{+} neurons.

Discussion

GRPergic signaling for cortex-wide communication

Neuropeptidergic signaling has been suggested to interconnect cortical neurons and provide control over cortical homeostasis and plasticity (Smith et al., 2019). This hypothesis is supported by the cellular specificity of receptor-ligand expression patterns but has largely not been tested functionally. Here, we provide direct evidence that distinct peptidergic cell-to-cell communication channels, consistent with those predicted by mRNA expression patterns, exist and regulate cortex-dependent behaviors. Unlike synaptic communication channels that have the ability to modulate individual cells through point-to-point communication, our data support that GRP acts on a larger scale through extrasynaptic diffusion (however, see ‘limitations of the study’ below). This mode of transmission for neuropeptides was proposed several decades ago (Agnati et al., 1986) and is thought to be a major communication mode for neuromodulators (Taber and Hurley, 2014).

Cortical GRPR signaling enhances fear memories

Neuromodulators are thought to mediate context-dependent control over functional cortical circuits (Marlin et al., 2015; Nakajima et al., 2014; Polack et al., 2013; Smith et al., 2019). We here provide evidence for a previously unknown peptidergic control mechanism of behaviorally-relevant cortical circuits. Our data suggest that GRP is released in a context-dependent manner to increase plasticity as needed to strengthen memories in the presence of aversive or threatening cues. Interestingly, although our tracing studies reveal that TeA receives strong direct synaptic drive from GRP+ amygdala projection neurons, inputs to primary ACx are non-synaptic, suggesting two distinct modes of action in these brain areas. We predict that the non-synaptic mode supports slower and longer-lasting modulation through activation of neuromodulatory receptors like GRPR, whereas the fast synaptic inputs to the TeA support stimulus-specific information transfer. State- or context-dependent release of GRP in the primary ACx cortex is thus optimal to broadly increase responses to and plasticity evoked by environmental stimuli without altering stimulus discriminability.

Our behavioral results showing impaired fear memory, but unchanged sound discrimination, support such a scenario.

VIP cells are recruited by novel sounds and shocks

Although it is generally accepted that VIP cells are important regulators of cortical disinhibition and plasticity (Fu et al., 2014, 2015; Karnani et al., 2016; Pfeffer et al., 2013; Pi et al., 2013), evidence for memory and learning enhancement by VIP cells is surprisingly scarce (Adler et al., 2019; Fu et al., 2015). VIP cell responses to sounds and aversive cues (air puffs) were observed previously in head-fixed animals (Pi et al., 2013), but it was unknown how VIP cells encode the changing valence of conditioned and unconditioned cues during fear conditioning. Interestingly, similar to amygdala VIP cells (Krabbe et al., 2019), we observed strong activation of VIP cells by unexpected shocks and habituation of VIP cell responses to shocks with learning of the sound-shock association. In contrast to amygdala VIP cells, however, we also observed strong responses to novel sounds, which later habituated, suggesting that the responses to unexpected sounds and shocks may facilitate association learning by releasing inhibition and thereby increasing plasticity in distal dendrites of glutamatergic neurons. Interestingly, a distinct type of disinhibitory neurons in L1 of the ACx also exhibits strong activation to shocks (Letzkus et al., 2011), suggesting that both cells act synergistically to disinhibit Pyr neurons (Letzkus et al., 2011). Furthermore, our data show that GRPR activation increases excitability of VIP cells *in vitro* and induction of IEG transcription *in vivo.* These data suggest that GRP-GRPR signaling leads to the observed memory enhancement by increasing non-discriminatory VIP cell responses, and thereby inducing plasticity in VIP cells that regulate disinhibition in a subset of glutamatergic neurons.

Towards a complete picture of neuromodulatory control of cortical circuits

The daunting task of unraveling the multitude of neuromodulatory effects on signal transmission and plasticity across all cortical cell types may be essential to understand how cortical function is modulated in different emotional/physiological states by the plethora of neuropeptide receptors (Smith et al., 2019; Tasic et al., 2016, 2018). The heterogeneity of expression patterns and the diversity of receptors per cell type (Smith et al., 2019; Tasic et al., 2016, 2018) offer a glimpse into how intricate and versatile neuromodulator effects in the cortex can be. Together with previous studies (Li et al., 2016a; Marlin et al., 2015; Nakajima et al., 2014)(Li et al., 2016a), our work underlines the importance for future studies to investigate additional cell type-specific neuromodulatory communication channels and their impact on network activity and behavior.

Limitations of the study

Although our experiments support a non-synaptic mode of transmission for GRP, we cannot exclude that point-to-point synaptic signaling by GRP also occurs. Thus, although our rabies virus experiments suggest only rare synaptic connectivity between GRP and VIP cells, these negative results might arise due to low efficiency of trans-synaptic transfer of rabies viruses at GRPergic synapses. In addition, we were not able to identify when GRP is released to modulate fear memories. This reflects a general gap in our understanding of neuropeptide signaling that results from two technical limitations: (1) a lack of understanding of the

activity patterns that efficiently drive peptide release; and (2) a lack of sensors with sufficient sensitivity to detect released peptide. Improved GRP sensors will be beneficial to identify detailed spatial and temporal release dynamics also under physiological conditions *in vivo.*

Our photometric recordings of VIP cells *in vivo* did not reveal significant changes following ablation of GRPR. However, the significantly reduced *Fos* expression in VIP cells lacking GRPR following fear conditioning suggests that more sensitive techniques, such as 2-photon Ca^{2+} imaging and opto-tagged extracellular recordings, might reveal how GRPR modulates VIP cell activity patterns *in vivo* and identify the network mechanisms through which GRP-induced VIP cell plasticity and activity modulate behavioral outcomes.

STAR METHODS

Resource Availability

Lead contact—Further information and requests for resources and reagents should be directed to and will be fulfilled by the Lead Contact, Bernardo L. Sabatini (bsabatini@hms.harvard.edu).

Materials availability—Plasmids in this study have been deposited to Addgene.

Data and code availability—Data reported in this paper will be shared by the lead contact upon request.

All original code has been deposited at Github and is publicly available from the lead contact upon request.

Any additional information required to reanalyze the data reported in this paper is available from the lead contact upon request.

Experimental model and subject details

The following mouse lines were used in this study: *Vip*-EGFP (Tg(Vip-EGFP)JN37Gsat, MMRRC Cat# 031009-UCD, RRID:MMRRC_031009-UCD (Gong et al., 2003)), *Sst*-EGFP (FVB-Tg(GadGFP)45704Swn/J, The Jackson Laboratory, IMSR Cat# JAX:003718, RRID:IMSR_JAX:003718 (Oliva et al., 2000)), *Pvalb*-EGFP (CB6-Tg(Gad1-EGFP)G42Zjh/J, The Jackson Laboratory, IMSR Cat# JAX:007677, RRID:IMSR_JAX:007677 (Chattopadhyaya et al., 2004)), *Vip-IRES-Cre* (VIPtm1(cre)Zjh/J, The Jackson Laboratory, IMSR Cat# JAX:010908, RRID:IMSR_JAX:010908 (Taniguchi et al., 2011)), Rbp4-Cre mice (Tg(Rbp4-cre)KL100Gsat, MMRRC Cat# 031125-UCD, RRID:MMRRC_031125-UCD (Gong et al., 2003)), mice harboring floxed *Grpr* (B6;129S7-$Grpr^{tm1Zfc}$/J, IMSR Cat# JAX:033148, RRID:IMSR_JAX:033148 (Yu et al., 2017)), $Grp^{-/-}$ KO mice (B6;129X1-Grp_{tm1Jfb}/ZfcJ, IMSR Cat# JAX:027593, RRID:IMSR_JAX:027593 (Zhao et al., 2013)) and *H2B-EGFP* mice (B6;129S4-Gt(ROSA)26Sortm2(CAG-HIST1H2BB/EGFP)Zjh/J, IMSR Cat# JAX:028581, RRID:IMSR_JAX:028581 (He et al., 2016)). The *Frt*-flanked STOP cassette was removed by previous crossing to an actin-Flp transgenic mouse line to obtain Cre-

dependent H2B-EGFP expression). C57BL/6J mice (The Jackson Laboratory, IMSR Cat# JAX:000664, RRID:IMSR_JAX:000664) were used as wild-type mice and for backcrossing. Transgene expression in *Vip*-EGFP mice was previously characterized in the hippocampus (Tyan et al., 2014)

All mice except for Sst-EGFP mice were backcrossed to C57BL/6J mice for at least 6 generations.

Mice of either sex were used at postnatal days 18 – 100.

Human tissue for FISH was obtained from The Stanley Medical Research Institute.

Animals used for *in vitro* experiments were group-housed, animals used for behavioral experiments were single-housed 4 to 7 days before start of the behavior. All mice were kept on a 12 h light/dark cycle. All experiments were conducted during the light phase of the schedule.

All procedures were performed in accordance with protocols approved by the Harvard Standing Committee on Animal Care following guidelines described in the U.S. National Institutes of Health Guide for the Care and Use of Laboratory Animals.

Method details

Plasmids—For the generation of the pAAV-CBA-DIO-GCaMP6s-P2A-mBeRFP-WPRE-pA plasmid, mRuby2-P2A was cut out from pAAV-CBA-FLEX-mRuby2-P2A-GCaMP6s via AgeI and NheI restriction sites and replaced by de novo synthetized Kozak-sequence via AgeI and NheI cloning sites:
GCTAGCCATACCATGATGATGATGATGATGAGAACCCATGGTGGCACCGGT. The STOP codon of GCaMP6s was then replaced by de novo synthetized GSG-P2A-mBeRFP via PCR cloning (Clone EZ):
GGAATTCTTATTAAAGTTTGTGCCCCAGTTTGCTAGGGAGGTCGCAGTATCTGGCC
ACAGCCACCTCGTGCTGCTCGACGGAGGTCTCTTTGTCGGCCTCCTTGATTCTTTC
CAGTCTTCTGTCCACATAGTAGACGCCGGGCATCTTGAGGTTCTTAGCGGGTTTCT
TGGATCTGTATGTGGTCTTGGCGTTGCAGATCAGGTGGCCCCCGCCCACGAGCTT
CAGGGCCATGTAGTCTCTGCCTTCCAGGCCGCCGTCAGCGGGGTACAGCATCTCG
GTGCTGGCCTCCCAGCCGAGTGTTTTCTTCTGCATCACAGGGCCGTTGGATGGGA
AGTTCACCCCTCTGATCTTGACGTTGTAGATGAGGCAGCCGTCCTGGAGGCTGGT
GTCCTGGGTAGCGGTCAGCACGCCCCCGTCTTCGTATGTGGTGGATCTCTCCCATG
TGAAGCCCTCAGGGAAGGACTGCTTAAAGAAGTCGGGGATGCCCTGGGTGTGGT
TGATGAAGGTCTTGCTGCCGTACATGAAGCTGGTAGCCAGGATGTCGAAGGCGAA
GGGGAGAGGGCCGCCCTCGACCACCTTGATTCTCATGGTCTGGGTGCCCTCGTAG
GGCTTGCCTTCGCCCTCGGATGTGCACTTGAAGTGGTGGTTGTTCACGGTGCCCT
CCATGTACAGCTTCATGTGCATGTTCTCCTTAATCAGCTCTTCGCCCTTAGACACCA
TAGGACCGGGGTTTTCTTCCACGTCTCCTGCTTGCTTTAACAGAGAGAAGTTCGT
GGCTCCGGATCC.

The sequence of the final construct was verified by sequencing.

pRSET-BeRFP plasmid was given to us by Zhihong Zhang (Yang et al., 2013). pAAV-CBA-FLEX-mRuby2-GSG-P2A-GCaMP6s-WPRE-pA was a gift from Tobias Bonhoeffer and Mark Huebener and Tobias Rose (Addgene plasmid # 68717) (Rose et al., 2016).

pcDNA3.1-mBeRFP was generated by cloning de novo synthetized mBeRFP into the pcDNA3.1(+) vector via BamHI-EcoRI cloning sites:
GCCACCATGGTGTCTAAGGGCGAAGAGCTGATTAAGGAGAACATGCACATGAAGC
TGTACATGGAGGGCACCGTGAACAACCACCACTTCAAGTGCACATCCGAGGGCG
AAGGCAAGCCCTACGAGGGCACCCAGACCATGAGAATCAAGGTGGTCGAGGGCG
GCCCTCTCCCCTTCGCCTTCGACATCCTGGCTACCAGCTTCATGTACGGCAGCAAG
ACCTTCATCAACCACACCCAGGGCATCCCCGACTTCTTTAAGCAGTCCTTCCCTGA
GGGCTTCACATGGGAGAGATCCACCACATACGAAGACGGGGGCGTGCTGACCGC
TACCCAGGACACCAGCCTCCAGGACGGCTGCCTCATCTACAACGTCAAGATCAGA
GGGGTGAACTTCCCATCCAACGGCCCTGTGATGCAGAAGAAAACACTCGGCTGG
GAGGCCAGCACCGAGATGCTGTACCCCGCTGACGGCGGCCTGGAAGGCAGAGAC
TACATGGCCCTGAAGCTCGTGGGCGGGGGCCACCTGATCTGCAACGCCAAGACC
ACATACAGATCCAAGAAACCCGCTAAGAACCTCAAGATGCCCGGCGTCTACTATG
TGGACAGAAGACTGGAAAGAATCAAGGAGGCCGACAAAGAGACCTCCGTCGAGC
AGCACGAGGTGGCTGTGGCCAGATACTGCGACCTCCCTAGCAAACTGGGGCACA
AACTTTAAT CRISPR/Cas9 plasmids were cloned at the Genome Engineering and iPSC Center (GEiC) at Washington University. Single guide RNAs (sgRNAs) were designed in Benchling, and in collaboration with the GEiC. The four sgRNAs that were tested *in vitro* at the GEiC targeted the second exon (first exon within coding sequence, within the first 285 nucleotides following the start codon) of *Grpr* (NM_008177.3) and were predicted to have high on- and low off-target cutting in Benchling and at the GEiC.

sgRNA-*Grpr1*: GATGATAAGCCCATAAACTGCNNGRRT

sgRNA-*Grpr2*: AACGACACCTTCAATCAAAGTNNGRRT

sgRNA-*Grpr3*: CAGGGATGACATAGATGAAGCNNGRRT

sgRNA-*Grpr4*: CTGCTGGTGACATGCGCCCCTNNGRRT

Out of these four tested sgRNAs targeting *Grpr*, we selected the one (referred to as sgRNA-*Grpr1*) with the lowest predicted off-target cutting efficiency, high on-target cutting efficiency in cultured neuroblastoma cells (42%), and strong functional reduction of $Ca2^{+}$ dynamics in ACx VIP cells.

The control sgRNA was designed in Benchling, targeted at the bacterial *lacZ* gene. We selected a sequence with no predicted on- and off-target cutting for *Mus musculus* coding DNA using Benchling analysis.

sgRNA-*lacZ*: CATCGCGTGGGCGTATTCGCA

sgRNAs were cloned into pAAV-CMV-Kozak-NLS-SaCas9-NLS-3xHA-Tag-pA-U6-sgRNA via BsaI cloning sites. This plasmid was a gift from Feng Zhang (Addgene plasmid # 61591) (Ran et al., 2015).

sgRNA-*Grpr1* and sgRNA-*Grpr2* were tested *in vivo* because of their high on-target cutting frequencies in cultured mouse neuroblastoma (N2a) cells (42% and 24% respectively) as confirmed by next-generation sequencing, and because of their low predicted off-target cutting. sgRNA-*Grpr2* excluded because of too low functional *Grpr* KO efficiency based on GCaMP6s imaging. sgRNA-*Grpr3* had high on-target cutting (64%), but was excluded because of high predicted off-target cutting. sgRNA-*Grpr4* was excluded because of too low on-target cutting efficiency in N2a cells (4%).

pcDNA3-mRuby2 was a gift from Michael Lin (Addgene plasmid # 40260) (Lam et al., 2012).

pAAV-EF1a-FAS-TdTomato (Addgene plasmid # 37092) (Saunders et al., 2012).

pAAV-CAG-GCAMP6s-WPRE-SV40 was a gift from Douglas Kim and GENIE Project (Addgene plasmid # 100844) (Chen et al., 2013).

pAAV-EF1a-Cre was a gift from Karl Deisseroth (Addgene plasmid # 55636) (Fenno et al., 2014).

pAAV CAG-DO-TC66T-mCherry plasmid was generated by restriction enzyme digest of pAAV-CAG-Flex-TC66T with SalI and AscI to cut out the inverted reading frame encoding TC66T-mCherry. The endings of TC66T-mCherry were then mutated to reverse the AscI and SalI restriction enzyme sites and the new insert SalI-TC66T-mCherry-AscI ligated into the original vector as a non-inverted reading frame. The CAG-Flex-TC66T plasmid was a gift from Liqun Luo (Addgene plasmid # 48331) (Miyamichi et al., 2013). pAAV-CAG-FLEX-oG-WPRE-SV40pA was a gift from Edward Callaway (Addgene plasmid # 74292) (Kim et al., 2016).

The following constructs were deposited to Addgene:

pAAV CBA-DIO-GCaMP6s-P2A-mBeRFP-WPRE-pA (RRID: Addgene_175177)

pAAV CAG-DO-TC66T-mCherry (RRID: Addgene_175178)

pcDNA3.1-BeRFP (RRID: Addgene_175173)

pX601-AAV-CMV::NLS-SaCas9-NLS-3xHA-bGHpa;U6::BsaI-sgRNA-lacZ (RRID: Addgene_175175)

pX601-AAV-CMV::NLS-SaCas9-NLS-3xHA-bGHpa;U6::BsaI-sgRNA-Grpr1 (RRID: Addgene_175176)

Immunohistochemistry—Mice were transcardially perfused with 4% paraformaldehyde (PFA). Coronal sections were cut at 50 μm thickness on a Leica VT 1000S Vibratome and washed with phosphate buffered saline (PBS). Free-floating sections were permeabilized and blocked for 1 hr with PBS containing 5% NGS and 0.2% Triton X-100. Incubation of the sections with primary antibodies was performed for 24 hrs at 4°C in fresh PBS containing 5% NGS and 0.2% Triton X-100. For double-labeling experiments both primary antibodies

were incubated simultaneously. Sections were washed with PBST 5x and incubated for 1 hr with 1:500 Alexa 647-goat anti-rabbit IgG (Invitrogen). After repeated washing with PBST and PBS, the sections were mounted on glass slides. Pictures were taken using a virtual slide microscope (Olympus VS120), a laser scanning confocal microscope (Leica TCS SP8) or a fluorescence microscope with structured illumination (Keyence, BZ-X710).

Primary Antibodies—1:5000 rabbit-anti Fos (Synaptic Systems Cat# 226 003, RRID:AB_2231974)

1:1500 rabbit anti HA-Tag (C29F4, Cell Signaling Technology Cat# 3724, RRID:AB_1549585)

1:500 chicken anti-GFP (Abcam Cat# ab13970, RRID:AB_300798)

Fluorescent *in situ* hybridization—Mice were deeply anesthetized with isoflurane and decapitated, and their brains were quickly removed and frozen in Tissue Tek OCT compound (VWR, Radnor PA) on dry ice. Brains were cut on a cryostat (Leica CM 1950) into 20 μm thick coronal sections, adhered to SuperFrost Plus slides (VWR, Radnor PA), and immediately refrozen. Samples were fixed in 4% paraformaldehyde for 15 min at 4 degrees, processed according to RNAscope Fluorescent Multiplex Assay manual (Advanced Cell Diagnostics, Newark CA), and coverslipped with ProLong antifade reagent (Molecular Probes, Eugene, OR). *Gad1* and *Gad2* probes were combined in one channel. *Slc17a6,7,8* were combined in one channel. *Sst* probe and *RabV-gp1* probe were diluted 1:1 and 1:200 respectively to avoid bleed through into other fluorescnece channels. For protease treatment, slices were incubated in Protease III for 20 min. CTB-labeled slices were treated with protease III for only 10 min to preserve endogenous CTB fluorescence. The following probes were used: Mm-*Fos* (#316921-C1 and 3), Mm-*Sst* (#404631-C1 and C3), Mm-*Pvalb* (#421931-C2 and C3), Mm- *Vip* (#415961-C1, C2 and C3), Mm-*Gad1* (#400951-C3), Mm-*Gad2* (#439371-C3), Mm-*Slc17a6* (#319171-C2), Mm-*Slc17a7* (#416631-C2), Mm-*Slc17a8* (#431261-C2), Mm-*Grp* (#317861-C1 and C3), Mm-*Grpr* (#317871-C2), V-*RabV-gp1* (#456781-C2 and C3 targeting rabies virus nucleoprotein N), *Cre* (#312281), Mm-*Crh* (#316091), Mm-*Npas4* (#423431), *oG* (#519441-C2), *SaCas9* (#501621-C3).

For FISH on human visual cortex slices, 14 μm thick fresh frozen sections were used. For protease treatment, slices were incubated in Protease IV for 40 min. Tissue was obtained from a white male, 53 years old, who died of a heart attack without known diseases. The following probes were used: Hs-*GRPR* (#460411-C1 and C3), Hs-*GRPR*-O1 (#465271-C1), Hs- *VIP* (#452751-C2), Hs-*GAD1* (#404031-C3).

Images were taken at a Leica SP8 X confocal microscope using a 63x 1.4 NA oil immersion objective (Harvard NeuroDiscovery Center), at a pixel size of 180 nm (or 240 nm for rabies tracing and *Fos* and *Npas4* analysis) and an optical section of 0.9 μm.

For cell type-specific quantification of *Grp* and *Grpr* expression levels, ROIs were drawn semi-automatically and manually optimized in ImageJ (RRID:SCR_003070). *Grp* and *Grpr* images were thresholded using either RenyiEntropy or a manually set threshold, and the

percent coverage of each ROI with *Grp* and *Grpr* puncta was quantified in ImageJ. Follow-up analysis was done in MATLAB (RRID:SCR_001622).

Stereotactic AAV injections—5-8 weeks old mice were surgerized. Anesthesia was induced with 5% isoflurane and maintained with 1-2.5% isoflurane. Ketoprofen (5-10 mg/kg) was given subcutaneously prior to incision. For injections, a small craniotomy (~ 1 mm diameter) was made using the following coordinates (distance from bregma [mm] / distance from midline [mm] / depth [mm] / angle [°]):

Motor cortex: 0.6 / 1.5 / 0.7

ACx: −3.25 / as lateral as possible / 0.9

TeA: 4.1 / as lateral as possible /1

Amygdala (LA, BLA): −1.8 / 3.4 / 4.2

Thalamus (MGN): 3.4 / 2.4 / 3.35

Thalamus (SG, MGM): 3.7 / 2.3 / 3.35

A glass micropipette was inserted through a small durotomy for virus delivery. The pipette was held in place for 10 min. 400 nl (200 nl in case of AAVretro and SG/MGM injections) AAV were injected at 40 nl/min using a UMP3 microsyringe pump (World Precision Instruments, Sarasota FL). The pipette was held in place for another 10 min after the end of the injection. The pipette was then slowly retracted. The scalp incision was sutured, and post-surgery analgesics were given to aid recovery for three days (5-10mg/kg ketoprofen injected subcutaneously every 24 hours). AAVs were allowed to express for at least 3 weeks before the mice were used for experiments.

The following AAVs and titers were used:

AAV2/2 pX601-AAV-CMV::NLS-SaCas9-NLS-3xHA-bGHpa;U6::BsaI-sgRNA-*Grpr1* (from Boston Children's hospital viral core, BCH): 1.01*10^13 GC/ml

AAV2/8 pX601-AAV-CMV::NLS-SaCas9-NLS-3xHA-bGHpa;U6::BsaI-sgRNA-*Grpr1* (from BCH): 3.6*10^12 GC/ml

AAV2/2 pX601-AAV-CMV::NLS-SaCas9-NLS-3xHA-bGHpa;U6::BsaI-sgRNA-*Grpr2* (from Boston Children's hospital viral core, BCH): 1.22*10^13 GC/ml

AAV2/2 pX601-AAV-CMV::NLS-SaCas9-NLS-3xHA-bGHpa;U6::BsaI-sgRNA-*lacZ* (from BCH): 1.67*10^12 GC/ml

AAV2/8 pX601-AAV-CMV::NLS-SaCas9-NLS-3xHA-bGHpa;U6::BsaI-sgRNA-*lacZ* (from Janelia viral core): 1.05*10^13 GC/ml

AAV2/2 hSyn-Cre-mCherry (from UNC Vector Core): 1.55*10^12 GC/ml

AAV2/DJ CBA-DIO-GCaMP6s-P2A-mBeRFP (from BCH): 1*10^12 GC/ml

AAV2/9 CAG-DIO-oG (BCH): 1*10^11 GC/ml

AAV2/9 CAG-DIO-TC66T-mCherry (BCH): 1*10^11 GC/ml

AAV2/8 CAG-DO-TC66T-mCherry (BCH): 1*10^11 GC/ml

AAV2/9 CAG-Flex-EGFP-WPRE-bGH (Penn Vector Core): 9.3*10^12 GC/ml

AAV2/1 hSyn grpLight1.2 (BCH): 10^9 GC/ml (neuronal culture): 4.13*10^12 GC/ml (*in vivo*)

AAV2/1 hSyn grpLight1.3 (BCH): 10^9 (neuronal culture); 1.6*10^13 GC/ml (*in vivo*)

AAV2/1 hSyn grpLight1.3ER (Vigene Biosciences): 10^9 GC/ml (neuronal culture)

AAVretro CAG-Cre (UNC vector core): 2.8*10^12 GC/ml

AAV2/2 EF1a DIO-hChR2(H134R)-mCherry-WPRE-pA (UNC Vector Core): 3.4*10^12 GC/ml

AAV2/9 hSyn-Cre-WPRE-hGH (Addgene #105553-AAV9; RRID:Addgene_105553): 1.1*10^12 GC/ml

AAVs from BCH were purified by iodixanol gradient purification and ultracentrifugation at 48krpm for 1 hr.

To avoid leak expression of Cre-dependent AAVs, all Cre-dependent AAVs were first injected into wild type mice at various titers to determine the titer at which no expression was detected in the control mice in the absence of Cre-recombinase.

Retrograde tracer injection (CTB)—6 to 8 weeks old wild type mice were injected into the ACx, motor cortex or auditory thalamus with 25-100 nl CTB 647 or CTB 555 (4 μg/μl, Molecular Probes, Eugene, OR). The surgery was as described above with the following changes: CTB was injected with a flow rate of 20 nl/min. The coordinates for the auditory thalamus were (in mm) −3.1 posterior to bregma, 2.2 lateral to midline, 3.3 deep. To avoid CTB leak into cortex after injections into the auditory thalamus, the pipette was retracted from the brain at around 2.75 μm per second.

10 days after injection, mice were sacrificed, and the brains used for *in situ* hybridization as described above. Images were taken at a Leica SP8 X confocal microscope using a 63x 1.4 NA oil immersion objective (Harvard NeuroDiscovery Center), a pixel size of 180 nm and an optical section of 0.9 μm.

Rabies virus tracing—EnvA-pseudotyped, glycoprotein-deleted rabies virus carrying nuclear localized EGFP transgene (SADΔG-H2B:EGFP(EnvA)) was generated in house, using starting materials from Byung Kook Lim (UCSD). The recombinant rabies viruses were generated as described previously (Mandelbaum et al., 2019) using protocols similar

to those established previously (Wickersham et al., 2010). In short, HEK 293T cells (ATCC Cat# CRL-11268, RRID:CVCL_1926) were transfected with pSPBN-SADΔG-H2B:EGFP (Mandelbaum et al., 2019), pTIT-B19N, pTIT-B19G, pTIT-B19L and pCAGGS-T7. Virions were then retrieved from the supernatant, amplified in BHK-B19G cells and concentrated through a serious of filtration and centrifugation steps. Pseudotyping was performed by infecting BHK-EnvA cells with virions from the previous step. Pseudotyped rabies virus titer was estimated based on serial dilution method (Osakada and Callaway, 2013), counting infected H2B:EGFP$^+$ HEK 293T-TVA800 cells and quantified as infectious units per ml (IU/ml). Pseudotyped rabies virus was used at a titer of approximately 1 x 10^9 IU/ml. For quality control, HEK 293T cells were infected with pseudotyped rabies virus at serial dilutions and H2B:EGFP$^+$ cells counted. The rabies virus batch used in this study had a leak of less than 2 x 10^3 IU/ml. Aliquots were stored at −80°C.

For transsynaptic retrograde tracing, 6-8 weeks old *Vip-IRES-Cre* mice were injected with 200 nl AAV2/9 CAG-DIO-TC^{66T}-mCherry encoding Cre-dependent avian receptor TVA with increased specificity (Miyamichi et al., 2013) and AAV2/9 CAG-DIO-oG (10^11 GC/ml each) (Kim et al., 2016) encoding Cre-dependent optimized glycoprotein into the auditory or motor cortex. The surgery was as described above. 3 weeks later, 200 nl SADΔG-H2B:EGFP(EnvA) was injected into the ACx or motor cortex as described above. Mice were sacrificed 7 days later and brains were sectioned on a cryostat for subsequent *in situ* hybridization or perfused and sliced on a vibratome for subsequent epifluorescent and confocal imaging. The following control injections were performed to verify specificity of rabies tracing:

200 nl SADΔG-H2B:EGFP(EnvA) was injected into the cortex to confirm specific specificity for TC^{66T}-expressing cells. No labeling was detected.

200 nl AAV2/8 CAG-DO-TC^{66T}-mCherry (Cre-off version of TC^{66T}, see Plasmids) and AAV2/9 CAG-DIO-oG (10^11 GC/ml each) were injected into the cortex of wild type mice followed by SADΔG-H2B:EGFP(EnvA) injections to confirm that oG expression was Cre-dependent in the presence of strong TC^{66T} and SADΔG-H2B:EGFP(EnvA) expression.

200 nl AAV2/9 CAG-DIO-TC^{66T}-mCherry and AAV2/9 CAG-DIO-oG (10^11 GC/ml each) were injected into the cortex of wild type mice followed by SADΔG-H2B:EGFP(EnvA) injections to confirm that TC^{66T} expression and SADΔG-H2B:EGFP(EnvA) transfection were Cre-dependent.

For *in situ* hybridization, every 4th section (20 μm thick) was used to identify and quantify starter cells defined by the expression of *Cre, oG* and the rabies-specific nucleoprotein N (*in situ* probe V-*RABV-gp1*). Endogenous mCherry expression (from AAV2/9 CAG-DIO-TC^{66T}-mCherry) was faint and diffuse due to tissue processing and could be clearly distinguished from in situ labeling (mCherry and *Cre* were imaged in the same channel). Endogenous EGFP fluorescence from SADΔG-H2B:EGFP(EnvA) rabies virus was strongly reduced due to tissue processing. The *in situ* probe V-*RABV-gp1* was therefore used to optimize detection of rabies virus. V-*RABV-gp1* and EGFP were imaged in the same channel. Every 4th section was used to identify and quantify retrogradely labeled cells

and *Grp* coexpression in the auditory thalamus using the *in situ* probes V-*RABV-gp1* and Mm-Grp. Every 8th cryostat section was used to identify and quantify retrogradely labeled cells and *Grp* coexpression in the cortex surrounding the injection site. Due to the high number of retrogradely labeled cells surrounding the injection site, we found this sampling rate to be adequate to analyze a sufficiently large number of cells. We normalized the number of retrogradely labelled cells to the number of detected starter cells.

The V-*RABV-gp1* probe was diluted 1:100 or 1:200 in probe diluent to avoid bleed through into other channels. The whole auditory and motor cortices were screened for starter cells. *Vip*$^{+}$ starter cells in the ACx were detected over a range of 400-720 μm (anterior-posterior axis). Retrogradely labeled cells after injections into the ACx were located in the ipsilateral and clACx, auditory thalamus and ipsilateral association cortices, but not in the LA, consistent with previous reports (Wall et al., 2016). To test whether *Grp* is expressed in neurons providing synaptic inputs to VIP cells, we detected neurons infected with RabV by FISH using the *RabV-gp1* probe, and analyzed *Grp* expression in *RabV-gp1*$^{+}$ cells. The numbers of identified starter cells was subtracted from the number of identified *RabV-gp1*$^{+}$ cells. *Grp* colabeling in retrogradely labeled cells was quantified in sections from 800 μm anterior to 800 μm posterior to the injection sites (ACx and M1), and in the entire auditory thalamus. The motor thalamus did not show high *Grp* labeling and was excluded from analysis.

Images were taken at a Leica SP8 X confocal microscope using a 63x 1.4 NA oil immersion objective (Harvard NeuroDiscovery Center), at a pixel size of 240 nm and an optical section of 0.9 μm. Cells were counted manually.

Optogenetic stimulation—For optogenetic stimulation experiments in acute slices, AAV2/2 EF1a DIO-hChR2(H134R)-mCherry-WPRE-pA and AAV2/9 hSyn-Cre-WPRE-hGH were stereotaxically co-injected into the amygdala (LA/BLA) and thalamus (MGN) as described above. Axons were stimulated in acute slices with 473 nm light (DPSS Laser System, Laserglow) at 20 mW through a 40x objective. To reveal direct synaptic amygdalo-cortical connections, TTX (1 μM) and 4-AP (100 μM) were added to the bath. Single 5 ms lasting pulses were used with 20 sec inter-trial interval. Postsynaptically recorded cells were patched with low Cl^{-} intracellular solution and kept at −70 mV holding potential. To test excitability of VIP cells in response to thalamic input stimulation, 1 sec bursts of 5 ms light pulses at 20 Hz were used once every 20 sec. 300 nM GRP were bath applied for 2 min after a 3 min baseline recording. VIP cells were patched with low Cl^{-} intracellular solution and held in current clamp to measure spontaneous and optogenetically evoked spikes.

Immediate early gene expression analysis—200 nl full-length mouse GRP (Phoenix Pharmaceuticals #027-40, 3 μM in NRR) or NRR (in mM: 135 NaCl, 5.4 KCl, 5 HEPES, 1.8 $CaCl_2$, pH 7.2 adjusted with KOH, sterile-filtered with 0.2 μm pore size) were injected into the right motor cortex of 6-8 week old male C57BL/6J, *Vip-IRES-Cre;Grpr*$^{wt/y}$ or *Vip-IRES-Cre;Grpr*$^{fl/y}$ mice. The surgery was performed as described above for AAV injections. Mice woke up from anesthesia within a few minutes after the end of the surgery and were allowed to move freely in their recovery chamber. 45 min after GRP or NRR were injection, mice were re-anesthetized, brains quickly dissected and frozen in OCT for *in situ*

hybridization as described above. For immunostaining, mice were perfused 1 1/2 hours after, and 50 μm thick coronal slices were cut on a vibratome for anti-FOS immunostaining (see protocol above).

Images of *in situ* hybridized tissue were taken at a Leica SP8 X confocal microscope equipped with a 63x 1.4 NA oil immersion objective (Harvard NeuroDiscovery Center), at a pixel size of 240 nm and an optical section of 0.9 μm. Confocal images of 460-470 μm width spanning all cortical layers were taken at a fixed distance from the midline from both hemispheres (2-3 slices per mouse, surrounding the injection site). ROIs were drawn manually around all stained *Vip*$^+$, *Sst*$^+$, *Pvalb*$^+$ and *Slc17a6/Slc17a7*$^+$ cells in ImageJ. *Fos* and *Npas4* images were thresholded manually. Slices were discarded if left and right hemisphere exhibited different background fluorescence. Percent coverage of each ROI with *Fos* or *Npas4* puncta was quantified in ImageJ.

Fos and *Npas4* expression levels in the left (uninjected) hemisphere were used as a baseline to account for variability in staining intensity and baseline *Fos* and *Npas4* expression. Data from both hemispheres are shown in most figures. Expression levels were defined as cell area covered with FISH labeling. Mean expression across cortical depth was calculated as average expression across sliding windows of 150 μm width for each slice. Cumulative distributions of *Fos* and *Npas4* expression in the right hemisphere were calculated by normalizing the expression of all cells of a defined cell type in the right hemisphere to the mean expression of *Fos* or *Npas4* in the same cell type in the left hemisphere (for each slice).

Due to the high excitability (and *Fos* induction) of ACx circuits upon damage of microvessels following glass pipette insertion, we limited our analysis to the motor cortex.

For *Fos* analysis in fear conditioned and naïve mice, all mice were injected into the ACx with CRISPR/Cas9 constructs targeting *Grpr* (one hemisphere) and *lacZ* (contralateral hemisphere) as described above. Right and left injections alternated such that both constructs were equally represented in each hemisphere. All mice were handled, housed and exposed to the behavioral fear conditioning boxes as described below, with the exception that naïve mice were never exposed to CS$^+$, CS$^-$ and shocks. All mice were anaesthetized directly after the fear conditioning session and the brains frozen for subsequent *in situ* hybridization for *Fos, Vip* and *SaCas9* (as described above). Images of primary ACx including the injection site were taken as described above. *SaCas9* labeling was used as an indication for successful injections (one mouse with weak *SaCas9* expression was excluded from analysis). ROIs were drawn manually around *Vip*$^+$ cells. Images were thresholded at a set threshold that was determined based on the background fluorescence across all images. *Fos* coverage per cell was quantified automatically in ImageJ and Matlab as described above. Staining and analysis were performed blind for CRISPR/Cas9 construct and behavioral testing protocol.

RNA sequencing analysis—Visual cortex RNA sequencing data were downloaded from the Allen Brain Institute:

https://portal.brain-map.org/atlases-and-data/rnaseq (Tasic et al., 2018)

http://casestudies.brain-map.org/celltax#section_explorea (Tasic et al., 2016)

Gene counts were normalized to counts per million (CPM). The two datasets were then screened for genes whose expression was correlated to *Vip* expression with a correlation coefficient of >0.5 in both datasets.

Electrophysiological recordings—For *in vitro* patch-clamp recordings, mice were deeply anesthetized with inhaled isoflurane, and transcardially perfused with ~30 ml ice-cold sucrose solution oxygenated with carbogen gas (95% O_2, 5% CO_2, pH 7.4). Mice were decapitated and brains removed. 300 μm thick sections were cut on a Leica VT 1000S vibratome in ice-cold oxygenated sucrose solution containing (in mM) 252 sucrose, 3 KCl, 1.25 $Na_2H_2PO_4$, 24 $NaHCO_3$, 2 $MgSO_4$, 2 $CaCl_2$, 10 glucose. Coronal slices were used for all experiments. Slices were incubated in oxygenated Ringer's extracellular solution containing (in mM) 125 mM NaCl, 25 mM $NaHCO_3$, 1.25 mM NaH_2PO_4, 2.5 mM KCl, 2 mM $CaCl_2$, 1 mM $MgCl_2$, 25 mM glucose at 32°C for ~15 min, and subsequently at RT until used for recordings. Whole-cell patch-clamp recordings were performed at 30-32°C using pipettes pulled from borosilicate glass capillaries with resistances of 3-4 MΩ. Sections were continuously perfused with oxygenated extracellular solution. Cells were visualized by an upright microscope equipped with Dodt gradient contrast and standard epifluorescence.

All electrophysiological recordings were acquired using Multiclamp 700B amplifier (Molecular Devices) MultiClamp Commander and MTTeleClient for telegraphs. MATLAB (RRID:SCR_001622) was used to control current/voltage output and to visualize and store acquired data. Signals were sampled at 10 kHz. Liquid junction potentials were not corrected. Patch clamp recordings were guided by a 60x/0.9NA LUMPlanFl/IR Olympus objective. Pipettes and microscope movements were controlled through MP-285 Sutter Instruments. The setup was equipped with a U-RFL-T Olympus fluorescence lamp.

Pyramidal cells were patched in wild type mice since their identification did not require EGFP labeling. Pyramidal cells were identified by their cell shape, localization, input resistance, membrane capacitance and firing pattern. All other cell types were identified based on EGFP expression in reporter mouse lines. Thus, VIP cells were identified in *Vip*-EGFP (Tg(Vip-EGFP)JN37Gsat) or *Vip-IRES-Cre x H2B-EGFP* mice, SST cells were identified in *Sst*-EGFP (FVB-Tg(GadGFP)45704Swn/J) mice and PVALB cells were identified in *Pvalb*-EGFP (CB6-Tg(Gad1-EGFP)G42Zjh/J) mice.

Inhibitory and excitatory postsynaptic currents (IPSCs and EPSCs) were recorded in identified cells voltage-clamped at −70 mV. For IPSCs, NBQX (10 μM, Tocris) and CPP (10 μM, Tocris) were added to the bath, and K^+-based, high Cl^- intracellular solution was used (in mM: 127.5 KCl, 11 EGTA, 10 Hepes, 1 $CaCl_2$, 2 $MgCl_2$, 2 Mg-ATP and 0.3 GTP, pH 7.3 adjusted with KOH). EPSCs were recorded with K^+-based low Cl^- intracellular solution (in mM: 130 K^+-Gluconate, 10 Hepes, 10 Phosphocreatine-Na, 10 Na-Gluconate, 4 ATP-Mg, 4 NaCl, 0.3 GTP, pH 7.2 adjusted with KOH) and gabazine (10 μM; SR 95531 hydrobromide, Tocris) was bath applied.

Series resistance was continuously monitored in voltage-clamp mode during PSC recordings measuring peak currents in response to small hyperpolarizing pulses. Recordings with series resistance changes of more than 20% were discarded. Series resistances of 35 MOhm were accepted for analyzing PSCs in interneurons and 25 MOhm were accepted for pyramidal cells.

Firing patterns were analyzed in current clamp mode applying 1 s current pulses with 3 s intersweep interval, starting at −200 pA and incrementally increasing the current by 20 pA steps until saturation of action potentials was reached (defined as a decrease in action potential amplitudes). Input resistance was calculated from the steady state voltage step to the first hyperpolarizing current injection for 1 s. Action potential (AP) half width was measured at half amplitude of the AP. Maximal frequency was measured at 1000 pA current injection or directly before saturation was reached. Rheobase was calculated as the minimal injected current that was required to elicit APs in whole-cell mode.

Membrane potential changes upon bath application of GRP (Phoenix Pharmaceuticals #027-40, 300 nM for 2 min if not indicated otherwise) was performed with K^+-based low Cl^- intracellular solution (see above) and with various drug cocktails using the following drugs and concentrations: NBQX (10 μM, Tocris), (R)-CPP (10 μM, Tocris), gabazine (10 μM; SR 95531 hydrobromide, Tocris), CGP55845 (10 μM, Tocris), TTX (1 μM, Tocris), $CdCl_2$ (100 μM, Sigma Aldrich) and BW2258U89 (10 μM, Phoenix Pharmaceuticals #027-22).

Current clamp recordings were downsampled to 1 kHz for all illustrations and for the analysis of responses to GRP. PSC frequency was calculated in sliding windows of 10 seconds, and baseline frequency was subtracted for each cell. Mean increase in PSC frequency and in membrane potential upon GRP bath application (300 nM for 2 min if not indicated otherwise) were calculated as difference between mean frequency or membrane potential during baseline and during a 3 min period starting at the time point when GRP reached the bath (based on TAMRA-GRP imaging, see below). A VIP cell was defined as responding to GRP if the mean membrane potential after GRP application was >2 SD above the mean baseline membrane potential and if the membrane potential change was larger than the maximal membrane potential change observed in response to 0 nM GRP.

MATLAB was used for of fline analysis of all data.

HEK 293T live-cell imaging—HEK 293T cells (ATCC Cat# CRL-11268, RRID:CVCL_1926) were transfected with the following plasmids (1.8 ng per well in a 24-well plate): pcDNA3-mRuby2, pAAV-EF1a-FAS-TdTomato, pAAV-CAG-GCAMP6s-WPRE-SV40, pcDNA3.1-mBeRFP. pAAV-CBA-DIO-GCaMP6s-P2A-mBeRFP and pAAV-EF1a-Cre were transfected at a 4:1 ratio.

Cells were imaged 48 hours post transfection. Culture medium was replaced and cells washed three times in imaging buffer (in mM): 125 NaCl, 2 MgCl2, 4.5 KCl, 10 glucose, 20 HEPES pH 7.4. Cells were continuously perfused with imaging buffer via a peristaltic pump. Cells were allowed to equilibrate in the new medium at room temperature until

fluorescence had reached a steady state (around 5-10 min). Live-cell imaging was performed at a Leica SP8 X confocal microscope (Harvard NeuroDiscovery Center). During the first imaging session, emission spectra were acquired at constant 473 nm excitation (405 nm excitation to image GCaMP at approximate isosbestic point). Images were taken at 390 to 770 nm emission wavelengths in 10 nm steps with 10 nm imaging bandwidth in a sequence of increasing wavelengths followed by a downward sequence (to balance bleaching effects). To test Ca^{2+} dependence of the fluorescence intensity, 2 mM $CaCl_2$ and 10 μM ionomycin (Sigma Aldrich) to promote calcium flux across membranes were added to the imaging buffer. 10 min after, fluorescence was stabilized and a second emission spectrum was acquired as described above.

For quantification of fluorescence changes upon Ca^{2+}/ionomycin flow-in, all emission spectra were normalized to the peak fluorescence in Ca^{2+}-free buffer. For each well, the area under the curve from 480 to 720 nm was calculated without and with Ca^{2+}.

To Compare GCaMP dynamics with and without coexpression of mBeRFP, emission spectra of pAAV-CAG-GCAMP6s-WPRE-SV40- and pAAV-CBA-DIO-GCaMP6s-P2A-mBeRFP-epxressing HEK 293T cells were acquired. Emission spectra were normalized to peak fluorescence at 480-560 nm emission wavelength in Ca^{2+}-free buffer and the area under the curve calculated from 480 to 560 nm without and with Ca^{2+}.

GCaMP-mBeRFP acute slice imaging—For GCaMP imaging upon GRP bath application, auditory or motor cortex of *VIP-IRES-Cre*, *VIP-IRES-Cre;Grpr*$^{wt/y}$ or *VIP-IRES-Cre;Grpr*$^{fl/y}$ mice were bilaterally injected with 10^{12} GC/ml AAV CBA-DIO-GCAMP-P2A-mBeRFP (400 nl) as described above. To test CRISPR/Cas9 AAVs, AAV CBA-DIO-GCAMP-P2A-mBeRFP was co-injected with AAV pX601-AAV-CMV::NLS-SaCas9-NLS-3xHA-bGHpa;U6::BsaI-sgRNA-*Grpr1, -Grpr2* or -*lacZ.*

Acute cortical slices were prepared as described for electrophysiological recordings. Slices were imaged with constant fluorescence excitation on an Olympus BX51WI using an Andor Ixon+ camera with Andor Solis Cell A imaging software using a 10x/0.3NA UMPlanFl Olympus objective. The setup was equipped with a U-RFL-T Olympus fluorescence lamp. Excitation filters in the U-MF2 imaging cubes were as follows: 472/30 nm (GCaMP and mBeRFP, Brightline). Emission filter: 520/35 nm (GCaMP), 650/100 nm (mBeRFP broad spectrum), 660/30 nm (reduced bleed through spectrum for mBeRFP: Semrock 3035B modified with FF01-660/30-25 emission filter). Since the GCaMP fluorescence was weak in acute slices at baseline, mBeRFP fluorescence was used to find healthy transfected cells. Each slice was allowed to equilibrate in the imaging chamber for 5 min before video acquisition started. Videos were taken at 32°C.

To verify Ca^{2+} independence of mBeRFP fluorescence in acute brain slices, cell-attached or whole-cell recordings were performed in GCaMP-mBeRFP-expressing VIP cells while videos of GCaMP and mBeRFP fluorescence (472/30 nm excitation and 660/30 nm emission) were acquired. Trains of action potentials were triggered by 10 Hz electrical stimulation for 5 s through the patch pipette. GCaMP and mBeRFP fluorescence were imaged at 5 Hz. Videos were saved as 8-bit TIFs. To image GCaMP at the approximate

isosbestic point, a fiber-optic-coupled LED (Thorlabs) was used to excite GCaMP at 405 nm through an optical fiber positioned in the proximity of the imaged cell. For quantifications, mBeRFP and GCaMP (405 and 472/30 nm excitation) mean ΔF/F was calculated during electrical stimulation (5 s duration), and mean mBeRFP and GCaMP (405 nm excitation) ΔF/F were normalized to mean GCaMP (472/30 nm excitation) ΔF/F.

To analyze calcium dynamics upon GRP application, after 3 min of baseline imaging, 300 nM GRP (if not indicated otherwise) were washed in for 2 min. GRP was washed out for 8 min before 50 mM KCl were bath applied. Video acquisition was stopped after maximum fluorescence was reached.

Video frames were corrected for movements of the slices using custom-written MATLAB software using semi-manual tracking of constant fluorescent markers on the slice.

A custom-written ImageJ script was used to calculate mean fluorescence in manually defined ROIs. Autofluorescence of the slice was calculated from an ROI outside of the injection site, and subtracted from the fluorescence signal. Fluorescence for every ROI was normalized to the peak fluorescence during KCl application to account for variability in GCaMP expression levels per cell. $\Delta F/F_{KCl}$ was then calculated by subtracting the average baseline fluorescence.

For quantification of average responses upon GRP application, mean $\Delta F/F_{KCl}$ was calculated over 3 min upon GRP bath application, starting with the time point when GRP arrived in the bath (based on TAMRA-GRP fluorescence, see below).

Responding cells were defined as cells with maximal $\Delta F/F_{KCl}$ increases upon GRP application of more than 2 SD above maximal $\Delta F/F_{KCl}$ during the baseline period. The start of $\Delta F/F_{KCl}$ increases after GRP application was defined as the first time point when $\Delta F/F_{KCl}$ increased above maximal baseline $\Delta F/F_{KCl}$+2 SD.

TAMRA-GRP imaging—TAMRA-GRP was custom-synthetized by Pepscan. TAMRA was attached to the N terminus of GRP. Peptide sequence: Val-Ser-Thr-Gly-Ala-Gly- Gly- Gly-Thr-Val-Leu-Ala-Lys-Met-Tyr-Pro-Arg-Gly-Ser-His-Trp-Ala-Val-Gly-His-Leu-Met-NH2. To test the delay of GRP flow-in on our system, non-fluorescent acute brain slices were imaged with a 650/100 nm emission filter. After 3 min baseline imaging, 300 nM TAMRA-GRP was bath applied for 2 min. The start of TAMRA-GRP arrival in the bath was defined as the first time point when fluorescence increased 2 SD above baseline fluorescence.

Sensor engineering and characterization—Sensor engineering and characterization were performed based on previously described protocols (Patriarchi et al., 2018). GRP sensor (grpLight) was generated by replacing intracellular loop 3 of human GRPR with circularly permuted GFP (cpGFP). The dynamic range and affinity of grpLight were optimized by changing the compositions of the linker between cpGFP and GRPR and of the intracellular loop.

The grpLight library was generated using circular polymerase extension cloning (CPEC). The variants were than introduced via PCR for final subcloning into pAAV.hSynapsin1 viral vectors. Active conformations of the sensors were predicted with rosetta_cm protocol of rosetta 3 (version 2015.31). For characterization in cells, HEK 293 cells (ATCC Cat# CRL-1573, RRID:CVCL_0045) were cultured and transfected as in (Patriarchi et al., 2018). Primary hippocampal neurons were freshly isolated and cultured as previously described (Patriarchi et al., 2018). Hippocampal neurons were virally transduced using AAVs (1×10^9 GC/ml) at DIV5, two weeks prior to imaging.

Cells were washed with HBSS (Life Technologies) supplemented with Ca^{2+} (2 mM) and Mg^{2+} (1mM) two times followed by time-lapse imaging with a 40X oil-based objective on an inverted Zeiss Observer LSN710 confocal microscope. For titration curves, apparent affinity (EC50) values were obtained by fitting the data with Hill Equation (Igor). ΔF/F in response to GRP at each concentration was calculated as $(F(t) - F_0) / F_0$ with $F(t)$ being the pixel-wise fluorescence value at each time, t, and either basal or averaged fluorescence prior to ligand application, F_0. Based on the ΔF/F maps, SNR was calculated as $\Delta F/F \times \sqrt{F_0}$ using a custom-made MATLAB script (Patriarchi et al., 2018).

pAAV hSyn grpLight1.2 was deposited to Addgene (RRID: Addgene_175174).

Cannula infusion—Cannulae were surgically implanted to locally infuse GRP into the cortex. Craniotomies were made as described for stereotactic injections. Stainless steel guide cannulae (26 gauge; C315GA/SPC, Plastics One, Roanoke, VA, USA) were positioned in cortical L1 1.9 mm medial to the fiber implantation site, tilted to the left with a 25 degree angle). The gap between the cannula and the skull was filled with a biocompatible transparent silicone adhesive (World Precision Instruments, Kwik-Sil) and allowed to dry for 10 min. The implant was secured with Loctite gel (#454). Hardening of the glue was accelerated by Zip Kicker (Pacer Technology). Dummy cannulae that did not extend beyond the guide cannulae (C315DC/SPC, Plastics One) were inserted to prevent clogging. Mice recovered for 3-4 weeks. For drug infusions, dummy cannulae were replaced by internal cannula (33 gauge; C315LI/SPC, Plastics One) that extended 1 mm beyond the guide cannulae and were connected to a pump. After a recovery time of 15 min, GRP and TAMRA-GRP (2 µl; 300 µM diluted in NRR) or NRR were infused at 100 nl/min. Note that TAMRA-GRP is a very inefficient GRPR ligand and was added to visualize the spread of GRP only. For simultaneous GCaMP imaging of sound/shock responses in VIP cells using photometry (see Methods below), baseline responses were measured 15 min after cannula insertion and directly before start of the infusion. GRP effects were measured 1 min after the first increase in red fluorescence was observed, indicating the presence of diffused GRP concentrations that reliably increase Ca^{2+} levels in VIP cells *in vivo.* CS^- was played 1 min after the CS^+/shock pairing. Note that due to fast desensitization of GRPR and fast habituation of VIP cells, sounds and shocks were presented and responses analyzed only during these two timepoints.

Fear conditioning—Mice were handled for 7 days, and single-housed for 5-7 days prior to fear conditioning. 2 days before fear conditioning, mice were habituated to the conditioning box for 10 min each day. The behavior boxes consisted of custom-built

white plexiglas boxes built around a shock grid floor (Med Associates # ENV-005A). The dimensions of the boxes were 40x30x40cm (WDH). The boxes were equipped with a normal light source (Med Associates # ENV-221CL), a near infrared light source (Med Associates # NIR-200), a speaker (Audax TW025A20) and a camera (Point grey # FL3-U3-13E4M-C and FL3-U3-13Y3M-C). Sound pressure levels were set to 55±1 dBA measured at the bottom of the behavioral box. The shock intensity was set to 0.6 mA consistent with a previous publication (Letzkus et al., 2011). The lights, the shock generator and playback of the sounds were controlled through an Arduino Uno. Sounds were played from an MP3 player (Sparkfun # DEV-12660) and amplified (Sparkfun #BOB-09816).

For fear conditioning, mice were placed into the rectangular box. Lights were switched on 2 min prior to the first sound, to record baseline activity levels. Each mouse was exposed to 15 repetitions of 2 different complex sounds at pseudorandom sequence with inter sound intervals of 60 to 130 sec (in average 82 sec). Each sound consisted of 30 sweeps (either upwards from 5 to 20 Hz or downwards from 20 to 5 Hz). Each sweep was 500 ms long and was followed by a 500 ms sound gap. Each sweep started and ended with a 50 ms ramp to prevent clicking noise of the speakers. Either upsweeps or downsweeps were chosen to serve as the conditioning sound and were paired to a 1 second lasting shock that coincided with the last sweep of the complex sound (conditioned sound, CS^+). The mice were pseudo-randomly allocated to the behavioral boxes and to the sounds such that the number of control and KO mice receiving either the up or the downsweep as CS^+ were balanced. Mice were video recorded at 30 frames per second and videos saved as compressed H.264 (AVC) video files.

On the retrieval day, mice were placed into the behavioral boxes equipped with round plastic walls. Light settings were changed to NIR only and the odor was changed to vanilla-odor to reduce contextual fear memory. Sounds were then played either in the same sequence as during the conditioning session or in an inverted sequence to exclude freezing differences inherent to the sequence of the sounds. No foot shocks were applied. This retrieval protocol is designed to test fear memory retrieval, and, unlike common extinction protocols that utilize long-lasting sounds or frequent sound repetitions during retrieval sessions, is not expected to result in significant fear extinction within a single session.

Analysis: Freezing was defined as ≥ 2 sec bouts of no movement other than breathing-related movements. Freezing behavior of mice was analyzed with custom-written MATLAB scripts. Freezing was detected based on calculated speed using centroid-based tracking. In brief, the video was thresholded manually, the centroid of the mouse determined for each frame. The speed threshold to detect freezing was semi-automatically determined by playback of video chunks of increasing speed levels until no movement was detected. All putative freezing bouts that were close to the threshold were then automatically played back in MATLAB and manually verified as freezing bouts or excluded. This step was crucial to distinguish between freezing bouts with strong rhythmic body movements due to heavy freezing-associated breathing, and bouts of slight movements including sniffing, certain types of grooming, slight twitching, and ear movements.

Freezing levels and speed during sounds was calculated for the first 29 sec of the sounds only, to exclude the time of the shock.

Discrimination index for the two sounds was calculated as follows: (freezing (CS^+) - freezing(CS^-)) / (freezing (CS^+) + freezing(CS^-)).

Histology: At the end of the experiments, mice were transcardially perfused with PBS and 4% paraformaldehyde. Brains were dissected and sliced on a vibratome (VT1000s, Leica) into 100 μm coronal slices for imaging endogenous fluorescence or 50 μm coronal slices for immunostainings as described above. Mice with spread of AAV-mediated expression into subcortical areas were excluded from the analysis.

Photometry:

Surgery: AAV-CBA-DIO-GCaMP-P2A-mBeRFP or AAVs encoding grpLight were injected as described above into the right hemisphere of the ACx. For *in vivo* imaging of amygdalo-cortical and thalamo-cortical neurons, AAVretro-CAG-Cre was injected into the ACx or ventral ACx/TeA and AAV-CBA-DIO-GCaMP-P2A-mBeRFP was injected into the amygdala (LA/BLA) or thalamus (SG/MGM), respectively. After virus injection, a syringe needle tip was used to scratch the skull for better adherence of the glue. Tapered fiberoptic cannula implants (MFC_200/230-0.37_2mm_MF1.25_A45; 5.5 mm for amygdala and thalamus) with low autofluorescence epoxy were implanted into the same craniotomy at 0.8-0.95 μm depth (ACx), 4.05 μm depth (amygdala) and 3.25 μm depth (thalamus), with the angled (uncoated) side of the fiber tip facing layers 2/3 of the ACx or backwards for amygdala and thalamus. The gap between the implant and the skull was filled with a biocompatible transparent silicone adhesive (World Precision Instruments, Kwik-Sil) and allowed to dry for 10 min. The implant was secured with Loctite gel (#454). Hardening of the glue was accelerated by Zip Kicker (Pacer Technology). The glue was painted with black nail polish to reduce amount of ambient light collected through the fiber implant.

Setup: A 200 μm diameter and 0.37 NA patchcord (MFP_200/220/900-0.37_2m_FCM-MF1.25, low autofluorescence epoxy, Doric) was used to connect fiber implants to a Doric filter cube for blue (465-480 nm) and red (555-570 nm) excitation light and with built-in photodetectors for green (500-540 nm) and red (580-680 nm) emission light (FMC5_E1(465-480)_F1(500-540)_E2(555-570)_F2(580-680)_S, Doric). Signals from the photodetectors were amplified with Doric amplifiers with a gain of 1-10x in DC mode and acquired using a Labjack (T7). LJM Library (2018 release) was installed to allow communication between MATLAB and Labjack through a USB connection. The voltage output from the LED drivers was amplitude modulated at 171 (470 nm excitation of GCaMP, mBeRFP and the GRP sensor) and 228 (565 nm excitation of TAMRA-GRP) Hz to filter out ambient light and bleed-through emission. Amplitude modulation was programmed in MATLAB. 470 nm LEDs (M470F3, Thorlabs; LED driver LEDD1B, Thorlabs) and 565 nm LEDs (M565F3, Thorlabs, LED driver LEDD1B, Thorlabs) were used. Light power at the patchcord tip was set to oscillate between 38 and 75 μW for 470 nm excitation and 23-38 μW for 565 nm excitation (min and max of the amplitude modulation sine wave).

For synchronization with behavior data, timestamps of each collected video frame as well as signals from the Arduino channels for light, shock and sound were collected with the Labjack synchronously.

Recordings: Mice were handled to fiber attachment for 7 days prior to behavioral training. Mice were allowed to move freely on the hand while cleaning the fiber implant with ethanol and while connecting the patchcord to the fiber implant. mBeRFP fluorescence was used to verify proper connection and stable fluorescence across days. We found that GCaMP and mBeRFP expression were stable after 4 weeks of expression, and thus all data were collected after at least 4 weeks of expression. Photometry data were sampled at 2052 Hz for all channels, and saved in 1 sec chunks. Collection started at least 10 secs before connection to determine autofluorescence from the patchcord. Since bleaching of GCaMP and mBeRFP were strongest during the first 2 days of recordings, photometry data from the 2 habituation sessions prior to fear conditioning were not used. On the following days, the first 10-30 sec of recordings after patchcord connection were discarded to exclude the initial drop in fluorescence due to bleaching and due to handling of the mouse each day. Traces with sudden drops in mBeRFP signal during the behavioral session pointed to detachment or coiling of the fiber and were discarded. To reduce bleaching during the behavioral settings, LEDs were switched off during sounds 6 to 10. Thereby we were able to achieve constant fluorescence levels on conditioning and retrieval day.

Analysis: Since the collected GCaMP/grpLight/mBeRFP fluorescence but not ambient light was amplitude-modulated by a 171 Hz sine wave, we analyzed GCaMP fluorescence by calculating the power at 171 ± 7.5 Hz using online and offline analysis with custom-written MATLAB scripts based on a previous publication (Owen and Kreitzer, 2019). Power of the fluorescence signals at 171 ±7.5 Hz was calculated over a 200 sample point sliding window with 180 sample point overlap. The resulting trace was corrected for bleaching: based on recordings from 3 mice without fluorophores, we found that the majority of bleaching during the behavioral sessions could be ascribed to autofluorescence bleaching. Therefore, we calculated an exponential fit for the minima of GCaMP and mBeRFP fluorescence traces (minima based on a sliding window of 5000 data points), corrected for the exponential drop and subtracted autofluorescence. Autofluorescence was measured in 3 implanted mice without fluorophores. We normalized GCaMP fluorescence to the mean expression level of mBeRFP. For Fig. S5J, GCaMP and mBeRFP fluorescence were instead normalized to minimal fluorescence levels at the end of the conditioning session to compare GCaMP and mBeRFP fluorescence and exclude movement artifacts.

Quantification and Statistical analysis

Normally distributed data with equal variance were compared using two-sample or paired t-tests, and data were shown as mean ± SEM. Normally distributed data with unequal variance were compared using the two-sample t-test for unequal variance and data were shown as mean ± SEM. Non-normally distributed data were compared using the Mann-Whitney-U test and data were shown as median (IQR). The Shapiro-Wilk test was used to test for normal distribution of data. Normally distributed data were tested for homogeneity of variance using

the F-test. P-values were corrected for familywise error rates with the Holm-Bonferroni test where applicable.

Behavioral data were compared using two-way ANOVA and Tukey's posthoc test if main interactions were significant.

Cumulative frequency distributions were compared using two-sample Kolmogorov-Smirnov tests. Graphs were made with custom-written scripts in MATLAB. The figures were assembled in Illustrator (Adobe). The following code was used for p-values in the figures: *<0.05; **<0.01; ***<0.001. The detailed statistics for all experiments can be found in the respective results sections and figure legends.

Supplementary Material

Refer to Web version on PubMed Central for supplementary material.

ACKNOWLEDGEMENTS

We thank Byung Kook Lim for providing starting material for rabies virus production, Zhou-Feng Chen for providing $GRPR^{fl/y}$ mice and the Genome Engineering and iPSC core at Washington University, Zhihong Zhang and Liqun Luo for providing plasmids. We thank Ivo Spiegel and Michael Greenberg for sharing unpublished data, Maree Webster for providing human tissue and the Neurobiology Imaging Center for consultation and instrument availability. This facility is supported by the Neural Imaging Center as part of a NINDS P30 Core Center grant (NS072030). We thank Dr. Barbara Caldarone for behavioral training via the Harvard NeuroDiscovery Center. We thank members of the Sabatini lab for feedback on the manuscript and Carolyn Marie Orduno Davis for assisting with grpLight *in vitro* characterization. The research was funded by grants from NIH R35NS105107 (BS), U01NS115579 (LT and BS), Q-FASTR, the Nancy Laurie Marks Foundation, Bertarelli Foundation, and postdoctoral fellowships from DFG, EMBO, the Ellen R. and Melvin J. Gordon Center for the Cure and Treatment of Paralysis, and the Brooks Foundation.

REFERENCES

Adler A, Zhao R, Shin ME, Yasuda R, and Gan WB (2019). Somatostatin-expressing interneurons enable and maintain learning-dependent sequential activation of pyramidal neurons. Neuron 102, 202–216.e7. [PubMed: 30792151]

Agnati LF, Fuxe K, Zoli M, Ozini I, Toffano G, and Ferraguti F (1986). A correlation analysis of the regional distribution of central enkephalin and β-endorphin immunoreactive terminals and of opiate receptors in adult and old male rats. Evidence for the existence of two main types of communication in the central nervous system: the volume transmission and the wiring transmission. Acta Physiol. Scand 128, 201–207. [PubMed: 3022556]

Batista-Brito R, Vinck M, Ferguson KA, Chang JT, Laubender D, Lur G, Mossner JM, Hernandez VG, Ramakrishnan C, Deisseroth K, et al. (2017). Developmental dysfunction of VIP interneurons impairs cortical circuits. Neuron 95, 884–895.e9. [PubMed: 28817803]

Boatman JA, and Kim JJ (2006). A thalamo-cortico-amygdala pathway mediates auditory fear conditioning in the intact brain. Eur. J. Neurosci 24, 894–900. [PubMed: 16930417]

Briggs F, and Usrey WM (2011). Corticogeniculate feedback and visual processing in the primate. J. Physiol 589, 33–40. [PubMed: 20724361]

Chattopadhyaya B, Di Cristo G, Higashiyama H, Knott GW, Kuhlman SJ, Welker E, and Huang ZJ (2004). Experience and activity-dependent maturation of perisomatic GABAergic innervation in primary visual cortex during a postnatal critical period. J. Neurosci 24, 9598–9611. [PubMed: 15509747]

Chen TW, Wardill TJ, Sun Y, Pulver SR, Renninger SL, Baohan A, Schreiter ER, Kerr RA, Orger MB, Jayaraman V, et al. (2013). Ultrasensitive fluorescent proteins for imaging neuronal activity. Nature 499, 295–300. [PubMed: 23868258]

Chiu C, Martenson J, Yamazaki M, Natsume R, Sakimura K, Tomita S, Tavalin S, and Higley M (2018). Input-Specific NMDAR-Dependent Potentiation of Dendritic GABAergic Inhibition. Neuron 97, 368–377.e3. [PubMed: 29346754]

Dalmay T, Abs E, Poorthuis RB, Hartung J, Pu DL, Onasch S, Lozano YR, Signoret-Genest J, Tovote P, Gjorgjieva J, et al. (2019). A Critical Role for Neocortical Processing of Threat Memory. Neuron 104, 1180–1194.e7. [PubMed: 31727549]

Fenno LE, Mattis J, Ramakrishnan C, Hyun M, Lee SY, He M, Tucciarone J, Selimbeyoglu A, Berndt A, Grosenick L, et al. (2014). Targeting cells with single vectors using multiple-feature Boolean logic. Nat. Methods 11, 763–772. [PubMed: 24908100]

Fu Y, Tucciarone JM, Espinosa JS, Sheng N, Darcy DP, Nicoll RA, Huang ZJ, and Stryker MP (2014). A cortical circuit for gain control by behavioral state. Cell 156, 1139–1152. [PubMed: 24630718]

Fu Y, Kaneko M, Tang Y, Alvarez-Buylla A, and Stryker MP (2015). A cortical disinhibitory circuit for enhancing adult plasticity. Elife 2015.

Gong S, Zheng C, Doughty ML, Losos K, Didkovsky N, Schambra UB, Nowak NJ, Joyner A, Leblanc G, Hatten ME, et al. (2003). A gene expression atlas of the central nervous system based on bacterial artificial chromosomes. Nature 425, 917–925. [PubMed: 14586460]

He M, Tucciarone J, Lee S, Nigro M, Kim Y, Levine J, Kelly S, Krugikov I, Wu P, Chen Y, et al. (2016). Strategies and Tools for Combinatorial Targeting of GABAergic Neurons in Mouse Cerebral Cortex. Neuron 91, 1228–1243. [PubMed: 27618674]

Hodge RD, Bakken TE, Miller JA, Smith KA, Barkan ER, Graybuck LT, Close JL, Long B, Johansen N, Penn O, et al. (2019). Conserved cell types with divergent features in human versus mouse cortex. Nature 573, 61–68. [PubMed: 31435019]

Iurilli G, Ghezzi D, Olcese U, Lassi G, Nazzaro C, Tonini R, Tucci V, Benfenati F, and Medini P (2012). Sound-driven synaptic inhibition in primary visual cortex. Neuron 73, 814–828. [PubMed: 22365553]

Jékely G, Melzer S, Beets I, Kadow ICG, Koene J, Haddad S, and Holden-Dye L (2018). The long and the short of it -A perspective on peptidergic regulation of circuits and behaviour. J. Exp. Biol 221.

Karnani MM, Jackson J, Ayzenshtat I, Sichani XH, Manoocheri K, Kim S, and Yuste R (2016). Opening holes in the blanket of inhibition: Localized lateral disinhibition by vip interneurons. J. Neurosci 36, 3471–3480. [PubMed: 27013676]

Kim EJ, Jacobs MW, Ito-Cole T, and Callaway EM (2016). Improved monosynaptic neural circuit tracing using engineered rabies virus glycoproteins. Cell Rep. 15, 692–699. [PubMed: 27149846]

Krabbe S, Paradiso E, d'Aquin S, Bitterman Y, Courtin J, Xu C, Yonehara K, Markovic M, Müller C, Eichlisberger T, et al. (2019). Adaptive disinhibitory gating by VIP interneurons permits associative learning. Nat. Neurosci 22, 1834–1843. [PubMed: 31636447]

Kroog GS, Jensen RT, and Battey JF (1995). Mammalian bombesin receptors. Med. Res. Rev 15, 389–417. [PubMed: 8531502]

Lam AJ, St-Pierre F, Gong Y, Marshall JD, Cranfill PJ, Baird MA, McKeown MR, Wiedenmann J, Davidson MW, Schnitzer MJ, et al. (2012). Improving FRET dynamic range with bright green and red fluorescent proteins. Nat. Methods 9, 1005–1012. [PubMed: 22961245]

Lee S, Kruglikov I, Huang ZJ, Fishell G, and Rudy B (2013). A disinhibitory circuit mediates motor integration in the somatosensory cortex. Nat. Neurosci 16, 1662–1670. [PubMed: 24097044]

Leinweber M, Ward DR, Sobczak JM, Attinger A, and Keller GB (2017). A sensorimotor circuit in mouse cortex for visual flow predictions. Neuron 95, 1420–1432.e5. [PubMed: 28910624]

Letzkus JJ, Wolff SBE, Meyer EMM, Tovote P, Courtin J, Herry C, and Lüthi A (2011). A disinhibitory microcircuit for associative fear learning in the auditory cortex. Nature 480, 331–335. [PubMed: 22158104]

Li K, Nakajima M, Ibañez-Tallon I, and Heintz N (2016a). A cortical circuit for sexually dimorphic oxytocin-dependent anxiety behaviors. Cell 167, 60–72.e11. [PubMed: 27641503]

Li P, Janczewski WA, Yackle K, Kam K, Pagliardini S, Krasnow MA, and Feldman JL (2016b). The peptidergic control circuit for sighing. Nature 530, 293–297. [PubMed: 26855425]

Lin Y, Bloodgood BL, Hauser JL, Lapan AD, Koon AC, Kim TK, Hu LS, Malik AN, and Greenberg ME (2008). Activity-dependent regulation of inhibitory synapse development by Npas4. Nature 455, 1198–1204. [PubMed: 18815592]

Mandelbaum G, Taranda J, Haynes TM, Hochbaum DR, Huang KW, Hyun M, Umadevi Venkataraju K, Straub C, Wang W, Robertson K, et al. (2019). Distinct cortical-thalamic-striatal circuits through the parafascicular nucleus. Neuron 102, 636–652.e7. [PubMed: 30905392]

Marlin BJ, Mitre M, D'Amour JA, Chao MV, and Froemke RC (2015). Oxytocin enables maternal behaviour by balancing cortical inhibition. Nature 520, 499–504. [PubMed: 25874674]

Merali Z, McIntosh J, Kent P, Michaud D, and Anisman H (1998). Aversive and appetitive events evoke the release of corticotropin-releasing hormone and bombesin-like peptides at the central nucleus of the amygdala. J. Neurosci 18, 4758–4766. [PubMed: 9614249]

Miyamichi K, Shlomai-Fuchs Y, Shu M, Weissbourd BC, Luo L, and Mizrahi A (2013). Dissecting local circuits: Parvalbumin interneurons underlie broad feedback control of olfactory bulb output. Neuron 80, 1232–1245. [PubMed: 24239125]

Mountney C, Sillberg V, Kent P, Anisman H, and Merali Z (2006). The role of gastrin-releasing peptide on conditioned fear: Differential cortical and amygdaloid responses in the rat. Psychopharmacology (Berl). 189, 287–296. [PubMed: 17033843]

Mountney C, Anisman H, and Merali Z (2008). Effects of gastrin-releasing peptide agonist and antagonist administered to the basolateral nucleus of the amygdala on conditioned fear in the rat. Psychopharmacology (Berl). 200, 51–58. [PubMed: 18563394]

Mountney C, Anisman H, and Merali Z (2011). In vivo levels of corticotropin-releasing hormone and gastrin-releasing peptide at the basolateral amygdala and medial prefrontal cortex in response to conditioned fear in the rat. Neuropharmacology 60, 410–417. [PubMed: 20974156]

Nakajima M, Görlich A, and Heintz N (2014). Oxytocin modulates female sociosexual behavior through a specific class of prefrontal cortical interneurons. Cell 159, 295–305. [PubMed: 25303526]

Oliva AA, Jiang M, Lam T, Smith KL, and Swann JW (2000). Novel hippocampal interneuronal subtypes identified using transgenic mice that express green fluorescent protein in GABAergic interneurons. J. Neurosci 20, 3354–3368. [PubMed: 10777798]

Osakada F, and Callaway EM (2013). Design and generation of recombinant rabies virus vectors. Nat. Protoc 8, 1583–1601. [PubMed: 23887178]

Owen SF, and Kreitzer AC (2019). An open-source control system for in vivo fluorescence measurements from deep-brain structures. J. Neurosci. Methods 311, 170–177. [PubMed: 30342106]

Patriarchi T, Cho JR, Merten K, Howe MW, Marley A, Xiong WH, Folk RW, Broussard GJ, Liang R, Jang MJ, et al. (2018). Ultrafast neuronal imaging of dopamine dynamics with designed genetically encoded sensors. Science 360, eaat4422. [PubMed: 29853555]

Pfeffer CK, Xue M, He M, Huang ZJ, and Scanziani M (2013). Inhibition of inhibition in visual cortex: The logic of connections between molecularly distinct interneurons. Nat. Neurosci 16, 1068–1076. [PubMed: 23817549]

Pi HJ, Hangya B, Kvitsiani D, Sanders JI, Huang ZJ, and Kepecs A (2013). Cortical interneurons that specialize in disinhibitory control. Nature 503, 521–524. [PubMed: 24097352]

Polack PO, Friedman J, and Golshani P (2013). Cellular mechanisms of brain state-dependent gain modulation in visual cortex. Nat. Neurosci 16, 1331–1339. [PubMed: 23872595]

Ran FA, Cong L, Yan WX, Scott DA, Gootenberg JS, Kriz AJ, Zetsche B, Shalem O, Wu X, Makarova KS, et al. (2015). In vivo genome editing using Staphylococcus aureus Cas9. Nature 520, 186–191. [PubMed: 25830891]

Roesler R, Meller CA, Kopschina MI, Souza DO, Henriques JAP, and Schwartsmann G (2003). Intrahippocampal infusion of the bombesin/gastrin-releasing peptide antagonist RC-3095 impairs inhibitory avoidance retention. Peptides 24, 1069–1074. [PubMed: 14499286]

Rose T, Jaepel J, Hübener M, and Bonhoeffer T (2016). Cell-specific restoration of stimulus preference after monocular deprivation in the visual cortex. Science 352, 1319–1322. [PubMed: 27284193]

Saunders A, Johnson CA, and Sabatini BL (2012). Novel recombinant adeno-associated viruses for Cre activated and inactivated transgene expression in neurons. Front. Neural Circuits 6.

Sheng M, McFadden G, and Greenberg ME (1990). Membrane depolarization and calcium induce c-fos transcription via phosphorylation of transcription factor CREB. Neuron 4, 571–582. [PubMed: 2157471]

Smith SJ, Smbül U, Graybuck LT, Collman F, Seshamani S, Gala R, Gliko O, Elabbady L, Miller JA, Bakken TE, et al. (2019). Single-cell transcriptomic evidence for dense intracortical neuropeptide networks. Elife 8.

Sun YG, and Chen ZF (2007). A gastrin-releasing peptide receptor mediates the itch sensation in the spinal cord. Nature 448, 700–703. [PubMed: 17653196]

Taber KH, and Hurley RA (2014). Volume transmission in the brain: Beyond the synapse. J. Neuropsychiatry Clin. Neurosci 26.

Taniguchi H, He M, Wu P, Kim S, Paik R, Sugino K, Kvitsani D, Fu Y, Lu J, Lin Y, et al. (2011). A resource of cre driver lines for genetic targeting of GABAergic neurons in cerebral cortex. Neuron 71, 995–1013. [PubMed: 21943598]

Tasic B, Menon V, Nguyen TN, Kim TK, Jarsky T, Yao Z, Levi B, Gray LT, Sorensen SA, Dolbeare T, et al. (2016). Adult mouse cortical cell taxonomy revealed by single cell transcriptomics. Nat. Neurosci 19, 335–346. [PubMed: 26727548]

Tasic B, Yao Z, Graybuck LT, Smith KA, Nguyen TN, Bertagnolli D, Goldy J, Garren E, Economo MN, Viswanathan S, et al. (2018). Shared and distinct transcriptomic cell types across neocortical areas. Nature 563, 72–78. [PubMed: 30382198]

Tervo DGR, Hwang BY, Viswanathan S, Gaj T, Lavzin M, Ritola KD, Lindo S, Michael S, Kuleshova E, Ojala D, et al. (2016). A designer AAV variant permits efficient retrograde access to projection neurons. Neuron 92, 372–382. [PubMed: 27720486]

Tyan L, Chamberland S, Magnin E, Camiré O, Francavilla R, Suzanne David L, Deisseroth K, and Topolnik L (2014). Dendritic inhibition provided by interneuron-specific cells controls the firing rate and timing of the hippocampal feedback inhibitory circuitry. J. Neurosci 34, 4534–4547. [PubMed: 24671999]

Wall NR, de la Parra M, Sorokin JM, Taniguchi H, Huang ZJ, and Callaway EM (2016). Brainwide maps of synaptic input to cortical interneurons. J. Neurosci 36, 4000–4009. [PubMed: 27053207]

Yang J, Wang L, Yang F, Luo H, Xu L, Lu J, Zeng S, and Zhang Z (2013). mBeRFP, an improved large stokes shift red fluorescent protein. PLoS One 8.

Yu YQ, Barry DM, Hao Y, Liu XT, and Chen ZF (2017). Molecular and neural basis of contagious itch behavior in mice. Science 355, 1072–1076. [PubMed: 28280205]

Zhang S, Xu M, Kamigaki T, Do JPH, Chang WC, Jenvay S, Miyamichi K, Luo L, and Dan Y (2014). Long-range and local circuits for top-down modulation of visual cortex processing. Science 345, 660–665. [PubMed: 25104383]

Zhao Z, Huo F, Jeffry J, Hampton L, Demehri S, Kim S, Liu X, Barry D, Wan L, Liu Z, et al. (2013). Chronic itch development in sensory neurons requires BRAF signaling pathways. J. Clin. Invest 123, 4769–4780. [PubMed: 24216512]

Highlights

- Gastrin releasing peptide (GRP) receptors are expressed in cortical VIP cells
- GRP modulates cortical disinhibitory VIP cell activity and gene expression
- Cortical VIP cells activate to novel sounds and shocks during fear conditioning
- Ablation of GRP receptor in auditory cortex results in impaired fear memory

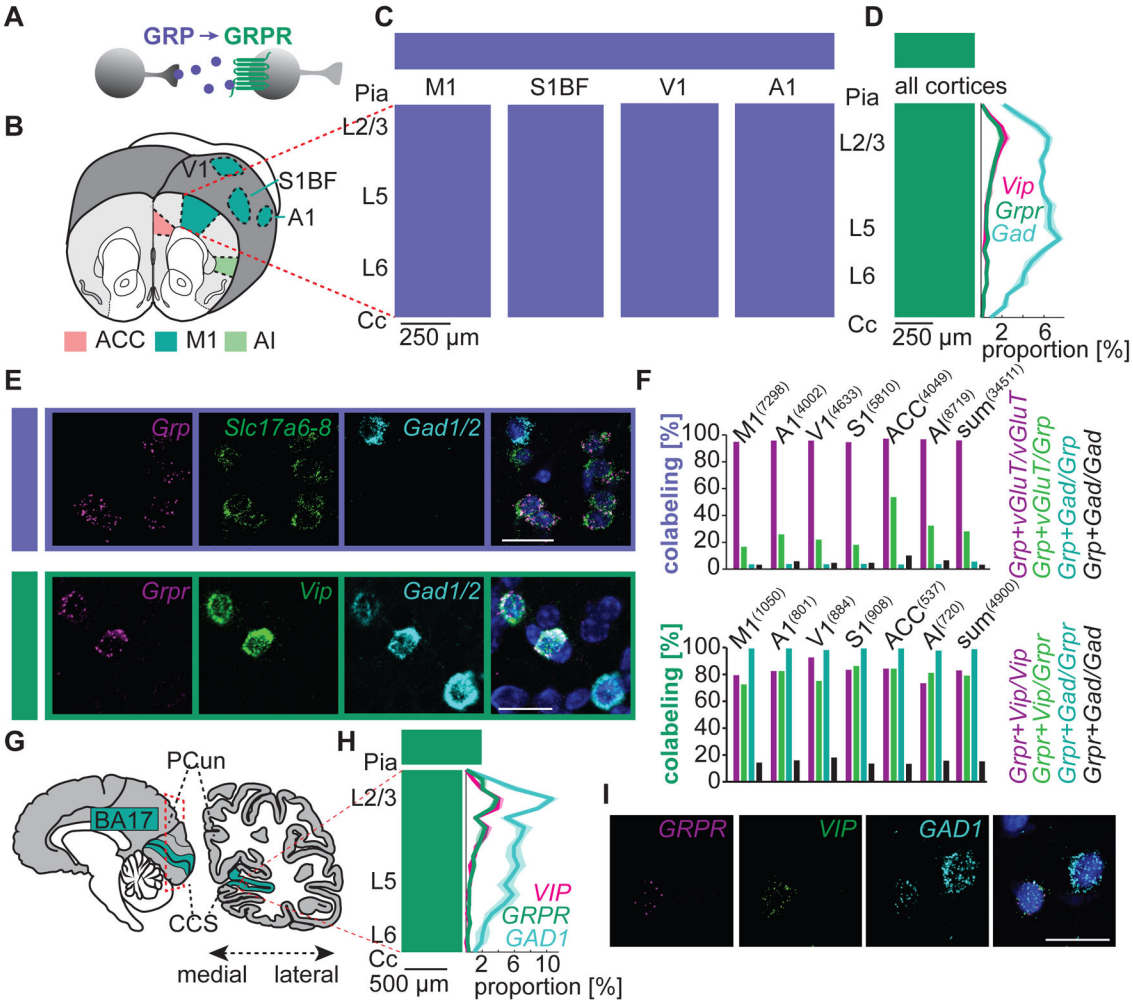

Fig. 1: Cortex-wide, cell type-specific expression of GRP and its receptor.

A, Schematic of GRP release and binding to GRP receptor (GRPR) in unidentified cell types.

B, GRP and GRPR expression were analyzed in mice in the indicated areas. Abbreviations: M1, primary motor; A1, primary auditory; V1, primary visual; S1BF, primary somatosensory – barrel field; ACC, anterior cingulate; AI, anterior insular cortex.

C, Locations of all identified *Grp*$^{+}$ cells in the indicated areas (n=5 slices for S1BF, V1, A1 and 7 for M1). see also Fig. S1.

D, Locations of all identified *Grpr*$^{+}$ cells in indicated areas (n=34 slices, 4900 cells). Quantification of the proportions (mean ± SEM) of cells that are *Grpr*$^{+}$, *Vip*$^{+}$ or *Gad*$^{+}$ across cortical depth (20 bins).

E, Representative confocal images of mouse cortex showing coexpression of *Grp* (*top*) and *Grpr* (*bottom*) with *Vip*, glutamatergic markers (*Slc17a6-8* encoding vGluT1-3) and GABAergic markers (*Gad1,2*). Scale bars, 20 µm.

F, Quantification of coexpression of *Grp* (*top*) and *Grpr* (*bottom*) with indicated genes. Numbers of analyzed cells per area are indicated above bars (≥15 slices from 4-7 hemispheres per area).

G, Schematic of human visual cortex (BA17) in which *GRPR* expression was analyzed using FISH.

H, *Left,* Locations of all identified *GRPR*$^+$ cells in 5 sections of human visual cortex. *Right,* Quantification of the proportions (mean ± SEM) of cells that are *GRPR*$^+$, *VIP*$^+$ and *GAD1*$^+$ (n=882 cells; 20 bins).

I, Representative confocal image of a *GRPR*$^+$/*VIP*$^+$/*GAD1*$^+$ human cell.

See also Fig. S1.

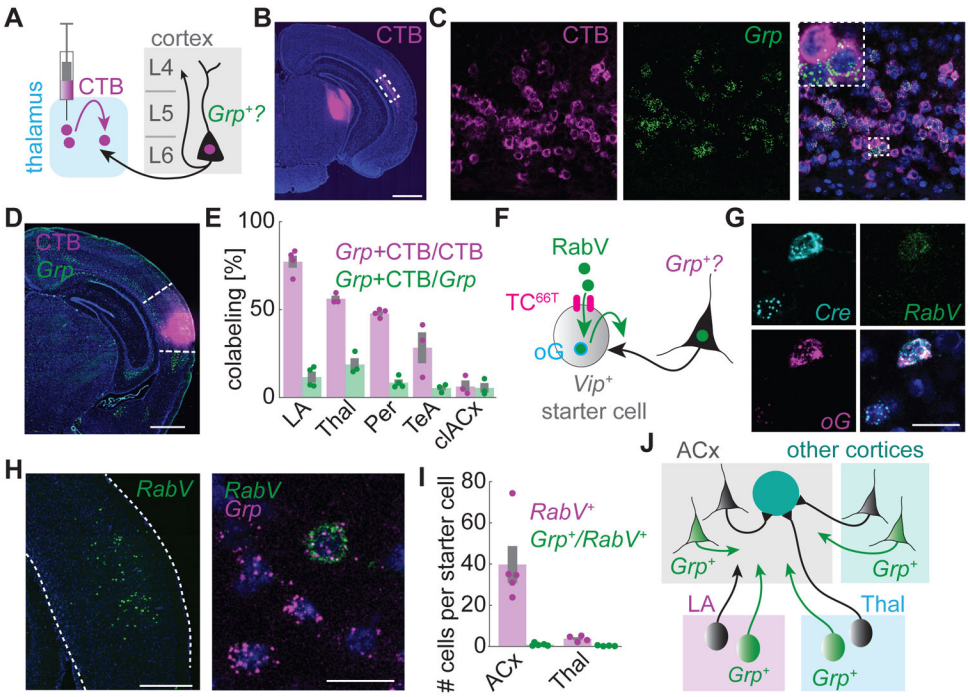

Fig. 2: Putative local and long-range sources of GRP

A, Schematic of retrograde tracing with CTB to quantify *Grp* expression in L6 cortico-thalamic neurons.

B, Representative epifluorescent image of CTB injection into auditory thalamus (Thal) and retrograde labeling in auditory cortex (ACx) L6.

C, Confocal image of retrogradely labeled cells in L6 of ACx and FISH against *Grp.* Inset: magnification of the highlighted area.

D, Retrograde tracing with CTB injected into ACx to quantify *Grp* expression in corticopetal projection neurons. Epifluorescent image of a representative injection and FISH against *Grp.*

E, Quantification of Grp^+ and CTB^+ cells in the indicated areas following injection as in D. Each dot represents data from one mouse. Mean ± SEM across 358-1142 CTB^+ cells per area. Abbreviations: LA, lateral amygdala; Per, perirhinal cortex; TeA, temporal association area; clACx, contralateral ACx.

F, Schematic of transsynaptic tracing from Vip^+ starter cells using pseudotyped rabies virus SADΔG-EnVA-H2B-EGFP (RabV).

G, Confocal image of an exemplary Vip^{Cre+} starter cell in ACx identified by *RabV-gp1* (RabV), *oG* and *Cre* (FISH).

H, Confocal images of $RabV\text{-}gp1^+$ cells in ACx (*left*) and of an exemplary $Grp^+/RabV\text{-}gp1^+$ cell (*right*).

I, Quantification of numbers of $RabV\text{-}gp1^+$ and Grp^+ cells after injections into ACx normalized to the numbers of starter cells. Each dot represents data from one mouse. Mean ± SEM.

J, Schematic of putative Grp^+ inputs to ACx VIP cells.

See also Fig. S2.

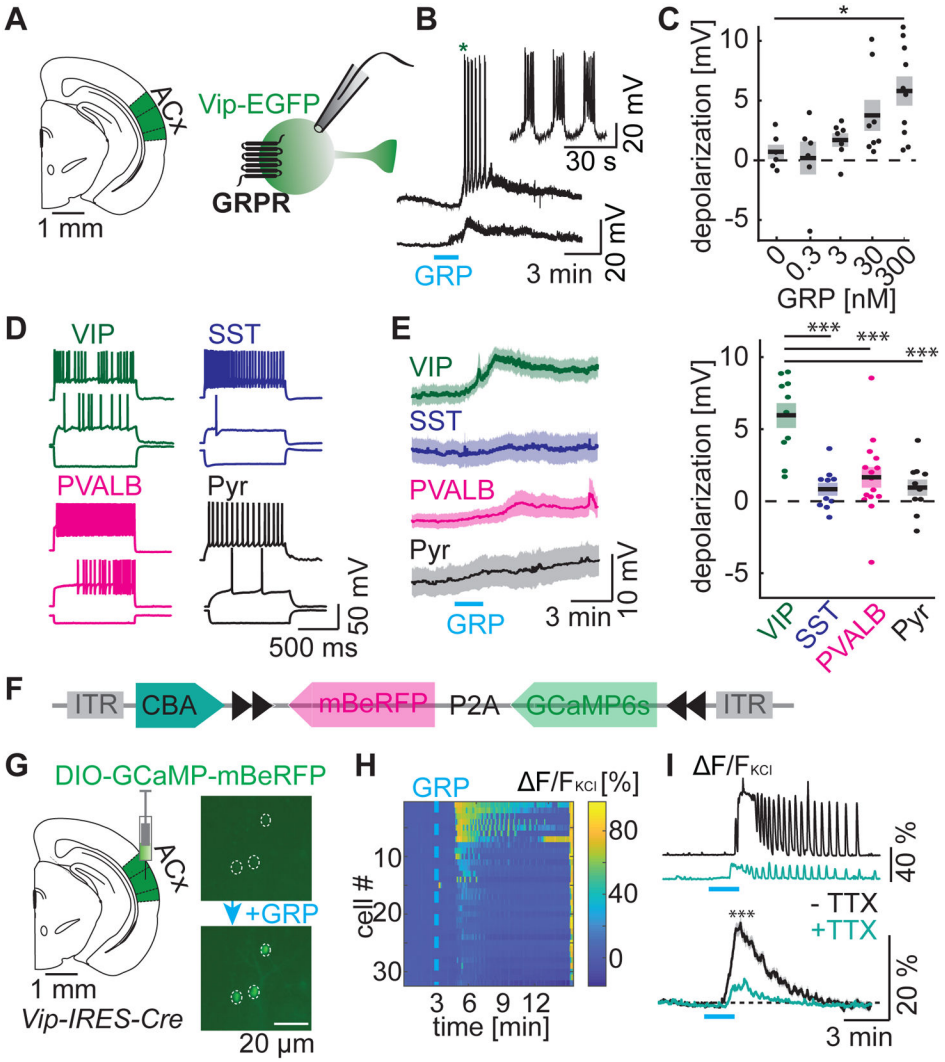

Fig. 3: GRP depolarizes and increases intracellular Ca^{2+} in cortical VIP cells

A, Schematic of whole-cell recording of ACx VIP cell used to examine effects of GRP.

B, Two exemplary VIP cells responding with bursts (*top*) or depolarization (*bottom*) following 2 min bath application of GRP (300 nM) in the presence of NBQX, CPP, gabazine, CGP. Inset: magnification of first bursts indicated by an asterisk.

C, Depolarization of VIP cells upon application of indicated concentrations of GRP. Mean ± SEM. 6-10 cells per group. Comparison 0 vs. 300 nM GRP: t-test for unequal variance: t(12.52)=3.76, p=0.01. Other comparisons n.s. Bath contains NBQX, CPP, gabazine, CGP.

D, Representative firing patterns of ACx VIP, SST, PVALB and pyramidal (Pyr) cells upon −200 pA current injection (*bottom*), at AP threshold (*middle*), and at maximal firing rate (*top*).

E, Average time course (*left*) and amplitude (*right*) of the membrane potential changes in each indicated cell type in ACx following GRP application. Bath contains NBQX, CPP, gabazine, CGP, TTX. Mean ± SEM. n=10 VIP, SST, Pyr cells and 15 PVALB cells. Comparison to VIP cells (Bonferroni-corrected t-test): SST: t(18)=−5.27, p<0.001; PVALB: t(23)=−3.83, p<0.001; Pyr: t(18)=−4.87, p<0.001.

F, Design of plasmid for Cre-dependent stoichiometric expression of GCaMP and mBeRFP for imaging of Ca^{2+} entry and detection of infected cells, respectively.
G, Injection of AAV DIO-GCaMP-P2A-mBeRFP into ACx of male Vip^{Cre} mice (*left*) and epifluorescent GCaMP imaging (*right*) in acute slices before (*top*) and after (*bottom*) GRP bath application, in the presence of NBQX, CPP, gabazine and CGP.
H, Heatmap of fluorescence changes (expressed relative to fluorescence following KCl application, $\Delta F/F_{KCl}$) across all imaged VIP cells in an exemplary acute ACx slice.
I, GCaMP fluorescence changes with or without TTX in two exemplary VIP cells (*top*) or across all recorded cells (*bottom*) in the presence of NBQX, CPP, gabazine and CGP. Mean ± SEM, Mann-Whitney U test: U=10178, $p<0.0001$. n=218 (−TTX) and 179 (+TTX) cells in 7 and 6 slices respectively.
See also Fig. S3.

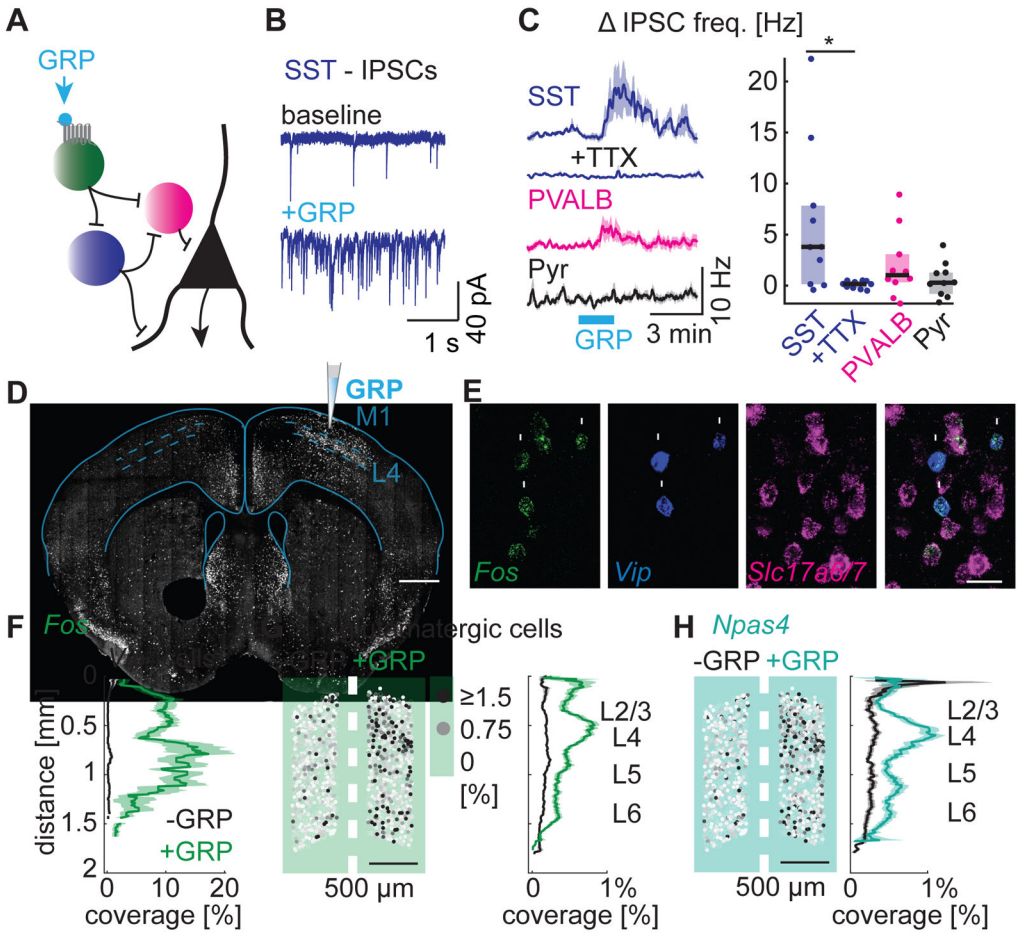

Fig. 4: GRP disinhibits cortex and induces IEG expression

A, Schematic of the disinhibitory circuit that underlies VIP cell function in cortex.

B, Whole-cell recordings of IPSCs in a representative SST cell in ACx before (*top*) and following (*bottom*) GRP application in the presence of NBQX and CPP.

C, Time courses (*left,* mean ± SEM) and magnitude (*right,* median and IQR) of IPSC frequency changes in SST, PVALB and Pyr cells (n=10 cells per group) in the presence of NBQX and CPP (TTX where indicated). Mann-Whitney U test: U=21, p=0.03.

D, Representative epifluorescent image of FOS immunostaining after injection of 3 µM GRP, as schematized, into the right motor cortex in anaesthetized mice.

E, Confocal images of *Fos* expression in *Vip*$^{+}$ (arrows) and glutamatergic cells (arrowheads) analyzed using FISH.

F-H, *Fos* and *Npas4* expression levels in *Vip*$^{+}$ and glutamatergic cells across all cortical layers for the right (green/turquoise) and left (black) motor cortices (mean ± SEM). Intensity-coded map of expression levels (% coverage) of all glutamatergic cells in an exemplary slice shown on the left (G, H). n=398 (*Vip*), 15108 (*Slc17a6,7*) cells, 3-5 mice for each condition and cell type.

See also Fig. S4.

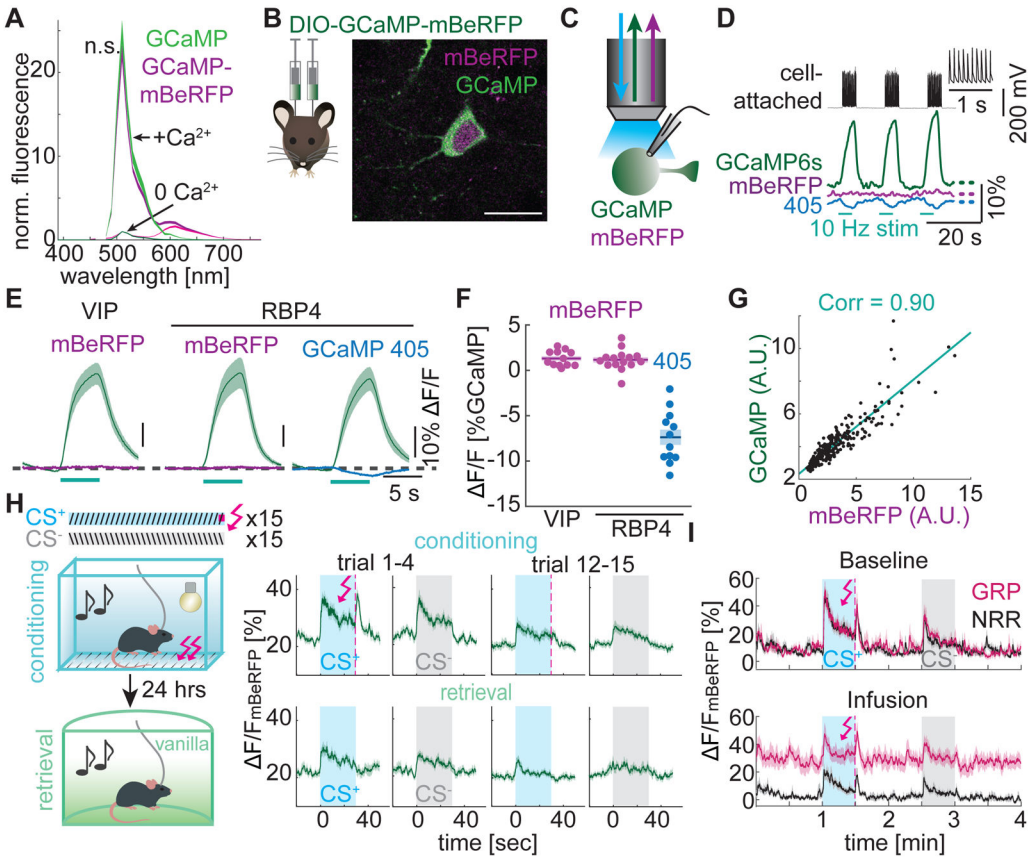

Fig. 5: ACx VIP cells encode novel sounds and shocks during fear conditioning

A, Fluorescence emission spectrum of GCaMP alone (green) and GCaMP-P2A-mBeRFP (magenta, pink) expressed in HEK 293T cells and measured with or without application of Ca^{2+}/ionomycin, indicating that mBeRFP does not interfere with GCaMP6s fluorescence. 2-sample t-test: t(10)=−0.12, p=0.91; n=6 wells each.

B, Confocal image of a Pyr cell after injection of AAV DIO-GCaMP-P2A-mBeRFP and AAV Cre into ACx.

C, Schematic of experimental setup for analysis of AP-dependent changes of GCaMP and mBeRFP fluorescence in acute brain slices during electrophysiological induction of spiking in VIP or L5 Pyr cells expressing GCaMP-P2A-mBeRFP in ACx of *Vip-IRES-Cre* and Rbp4-Cre mice.

D, AP bursts (each 5 s at 10 Hz) induced in an exemplary $RBP4^+$ neuron through a cell-attached electrode (top) with GCaMP and mBeRFP fluorescence (473 nm excitation, *middle*) and GCaMP fluorescence (405 nm excitation, *bottom*). Inset shows individual spikes from the last burst.

E, Average GCaMP and mBeRFP (473 nm excitation) and GCaMP (405 nm excitation) fluorescence changes (ΔF/F). Data from cell-attached and whole-cell recordings were pooled. Dashed line: baseline fluorescence. Mean ± SEM from n≥3 mice each; n=12 VIP, 15 RBP4 GCAMP/mBeRFP, and 12 RBP4 GCaMP (405 nm) cells.

F, Quantification of fluorescence changes shown in E normalized to GCaMP (473 nm) fluorescence change. mBeRFP fluorescence was largely unaffected by neuronal activity. In comparison, GCaMP fluorescence was reduced when excited at 405 nm (−7.4±0.8%).
G, Correlation of GCaMP and mBeRFP fluorescence in *Vip*$^{+}$ cells after injection of AAV DIO-GCaMP-P2A-mBeRFP into ACx of *Vip-IRES-Cre* mice (linear regression and correlation coefficient in cyan). n=335 cells from 3 injection sites.
H, GCaMP fluorescence changes measured in ACx VIP cells around presentation of conditioned (CS^{+}, blue) and unconditioned sounds (CS^{-}, grey) and shocks (dashed pink lines) early (trial 1-4) and late (trial 12-15) on the conditioning (top) or retrieval (bottom) day. n=11 mice.
I, GCaMP fluorescence changes measured around presentation of CS^{+} (blue) and CS^{-} (grey) and shocks (dashed pink lines) before (*top*) and following (*bottom*) infusion of GRP (pink) or control solution (NRR, black). n=8 (GRP) and 7 (NRR) mice.
Data in A, F-I: Mean ± SEM.
See also Fig. S5.

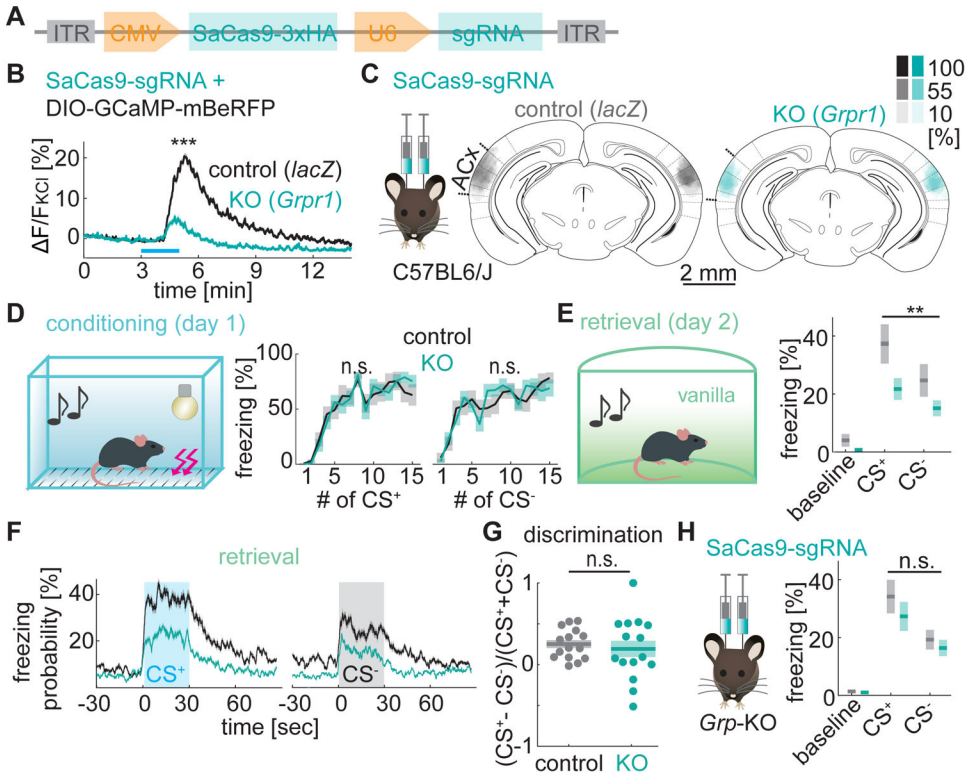

Fig. 6: GRPR signaling in the ACx enhances fear memories

A, Design of the plasmid for CRIPSR/Cas9-mediated KO of *Grpr* (here abbreviated as SaCas9-sgRNA) (Tervo et al., 2016).

B, GCaMP fluorescence changes measured in acute slices upon GRP application for VIP cells expressing GCaMP-P2A-mBeRFP and SaCas9-sgRNA targeting either *Grpr* (KO, *Grpr1*) or *lacZ* (ctrl). Mann-Whitney U test: U=25956; p<0.0001; n=602 and 298 cells in 10 (ctrl) and 9 (KO) slices.

C: Quantification of bilateral SaCas9-HA expression after injection of SaCas9-sgRNA targeting *lacZ* (ctrl, grey) or *Grpr* (KO, turquoise). See Fig. S6 for analysis of expression in the whole brain. Color-code: % of mice with SaCas9-HA expression.

D, Auditory fear acquisition, measured as the percentage of time spent freezing during presentation of 15 CS^+ and CS^- on conditioning day (histology shown in C). 2-way ANOVA, main effect of genotypes: CS^+: p=0.90, F=0.01; CS^-: p=0.78, F=0.08, no significant interaction of genotype and stimulus number. N=15 mice per group.

E, Auditory fear memory retrieval, measured as the percentage of time spent freezing averaged across 15 presentations of CS^+ and CS^- on the retrieval day. 2-way ANOVA: main effect of genotype: p=0.01, F=6.41, no significant interaction of genotype and stimulus (CS^+ vs CS^-).

F, Time courses of average freezing probability across all CS^+ and CS^- during fear memory retrieval.

G, Sound discrimination indices measured during retrieval. T-test for unequal variance: t(20.13)=0.53, p=0.60.

H, Auditory fear memory retrieval in CRISPR/Cas9-expressing *Grp*$^{-/-}$ KO mice, measured as the percentage of time spent freezing averaged across 15 presentations of CS^+ and CS^- on the retrieval day. 2-way ANOVA: main effect of genotype: p=0.28, F=1.21, no significant interaction of genotype and stimulus (CS^+ vs CS^-), n = 14 mice per group.
All summary data shown as Mean ± SEM.
See also Fig. S6.

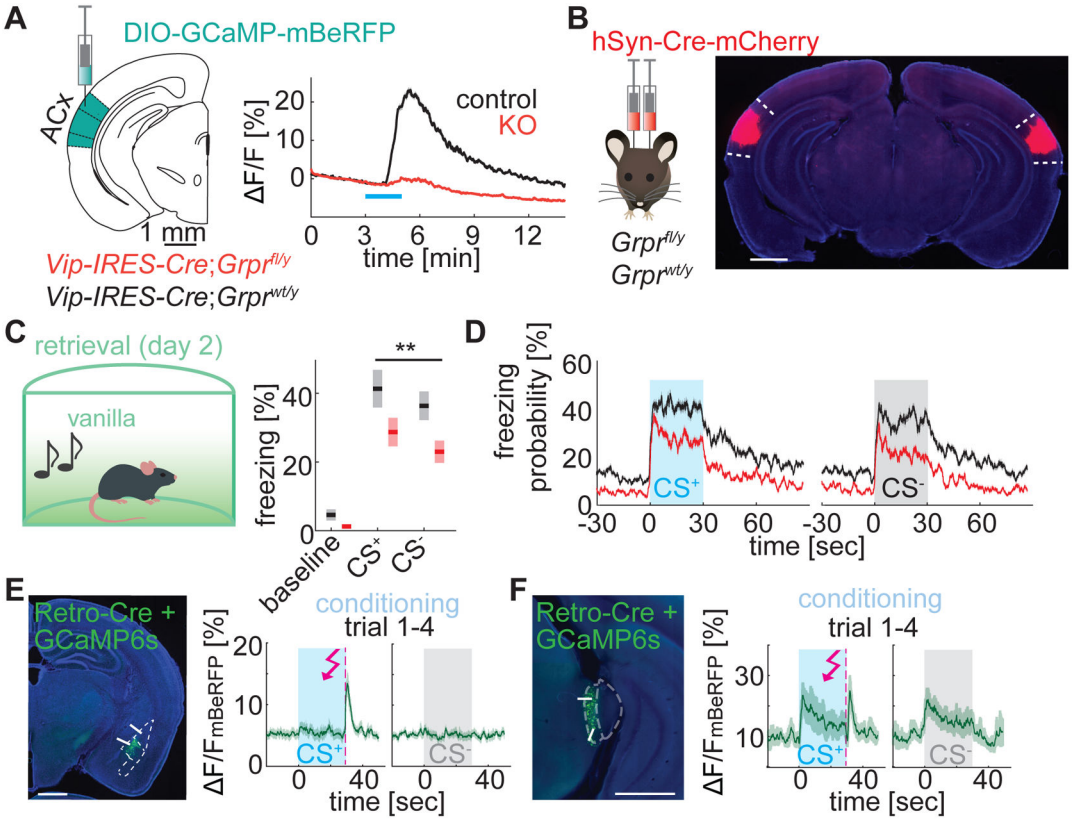

Fig. 7: Impaired fear memory in mice with conditional KO of GRPR in the ACx

A, GCaMP fluorescence changes in VIP cells following GRP application in acute ACx slices from ctrl mice (*Vip-IRES-Cre;Grpr*$^{wt/y}$) or mice lacking GRPR in VIP cells (*Vip-IRES-Cre;Grpr*$^{fl/y}$). Two-sample t-test: t(1178)=26.97, p<0.0001, n=655 cells in 14 slices (ctrl) and 525 cells in 11 slices (KO).

B, Injection of AAV hSyn-Cre-mCherry into ACx of *Grpr*$^{wt/y}$ or *Grpr*$^{fl/y}$ mice to locally KO *Grpr*. Right: Epifluorescent image of exemplary injection sites. Quantification of expression levels across all mice: Fig. S7.

C, Time spent freezing during fear memory retrieval in *Grpr*$^{wt/y}$ (ctrl) and *Grpr*$^{fl/y}$ (KO) mice injected into ACx with AAV encoding Cre-mCherry. 2-way ANOVA: main effect of genotype: p=0.004, F=8.99, no significant interaction of genotype and stimulus (CS^+ vs CS^-). N=14 mice per group.

D, Time course of average freezing probability across all CS^+ and CS^- presentations during fear memory retrieval.

E, Photometric recordings from LA/BLA projection neurons, retrogradely tagged with AAVretro-Cre injections into the ACx. GCaMP fluorescence changes measured during CS^+ (blue), CS^- (grey) and shocks (dashed pink lines) during early conditioning trials (trial 1-4). n=10 mice.

F, Photometric recordings from thalamic SG/MGM projection neurons, retrogradely tagged with AAVretro-Cre injections into the ventral ACx and TeA. GCaMP fluorescence changes measured during early conditioning trials (trial 1-4). n=5 mice.

All summary data shown as Mean ± SEM.

See also Fig. S7.